Title: Optimization of systemic AAV9 gene therapy in Niemann-Pick disease, type C1 mice

Running Title: Systemic AAV9 gene therapy in *Npc1*^{m1N} mice

Summary Blurb: Systemic AAV9-h*NPC1* gene therapy in null *Npc1*^{m1N} mice at higher doses or with earlier administration and treatment of hypomorphic *Npc1*^{I1061T} mice delays disease progression and increases lifespan.

Authors: Avani V. Mylvara[1,2*], Alana L. Gibson[2,3*], Tansy Gu[2,4*], Cristin D. Davidson[1,2+], Arturo A. Incao[2], Katerina Melnyk[1], Susan R. Gembic[1], Dominick Pierre-Jacques[5], Stephanie M. Cologna[5], Charles P. Venditti[2], Forbes D. Porter[1], William J. Pavan[2]

[1]*Eunice Kennedy Shriver* National Institute of Child Health and Human Development, National Institutes of Health, Department of Human Health and Services, Bethesda, MD; [2]National Human Genome Research Institute, National Institutes of Health, Department of Human Health and Services, Bethesda, MD; [3]Howard Hughes Medical Institute, Department of Cellular and Molecular Medicine, Section of Neurobiology, Division of Biological Sciences, University of California, San Diego, San Diego, CA; [4]University of North Carolina, Chapel Hill, NC; [5]University of Illinois Chicago, Chicago, IL
*Indicates equal contribution

Author Contributions

- AVM – data curation, formal analysis, investigation, methodology, validation, visualization, writing – original draft, writing – reviewing & editing (0000-0002-8741-4008)
- ALG – data curation, formal analysis, investigation, validation, writing – reviewing & editing (0000-0003-2247-7064)
- TG – data curation, formal analysis, investigation, validation, writing – reviewing & editing (0000-0002-0653-0892)
- CDD – conceptualization, data curation, investigation, project administration, supervision, validation, visualization, writing – original draft, writing – reviewing & editing (0000-0002-5508-8113)
- AAI – investigation, methodology (0000-0001-6801-4562)
- KM – formal analysis, investigation, validation, visualization, writing – reviewing & editing (0000-0001-9167-5801)
- SG – formal analysis, investigation, validation, writing – reviewing & editing
- DP-J – data curation, formal analysis, investigation, methodology, visualization, writing -reviewing & editing (0009-0009-1272-0607)
- SMC – conceptualization, funding acquisition, methodology, project administration, resources, supervision, writing – reviewing & editing (0000-0002-3541-3361)
- CPV – methodology, ideas, writing – reviewing & editing (0000-0001-6599-1253)
- FDP – project administration, supervision, funding acquisition, resources, writing – review & editing (0000-0001-9397-0046)
- WJP – conceptualization, project administration, supervision, funding acquisition, resources (0000-0001-8281-5120)

[+]Corresponding Author (Cristin Davidson)

Abstract:

Niemann-Pick disease, type C1 (NPC1) is a rare, fatal neurodegenerative disorder caused by pathological variants in *NPC1*, which encodes a lysosomal cholesterol transporter. FDA-approved treatments are limited and do not target the underlying genetic defect. Both systemic and central nervous system (CNS) delivery of AAV9-h*NPC1* have shown significant disease amelioration in NPC1 murine models. To assess the impact of dose in null $Npc1^{m1N/m1N}$ mice, we systemically administered three different doses of AAV9-h*NPC1* at 4 weeks old. Then, to assess the impact of age, we administered the medium dose before phenotypic onset or at early- or late-stage of disease progression (4, 6 or 8 weeks old, respectively). Higher vector doses and earlier treatment were associated with significantly increased lifespan, slower disease progression, and enhanced CNS transduction. In $Npc1^{I1061T/I1061T}$ mice, a model recapitulating a common human hypomorphic variant, similar benefits ensued. Our findings help define dose ranges, treatment ages, and efficacy in hypomorphic models of NPC1 deficiency and suggest that higher doses of AAV9-h*NPC1* in pre-symptomatic disease states are likely to yield better outcomes in NPC1 individuals.

Introduction:

Niemann-Pick disease, type C (NPC) is a rare, fatal neurodegenerative disease with an incidence of ~1 in 100,000 live births [1]. This autosomal recessive lysosomal storage disorder is marked by unesterified cholesterol and sphingolipid accumulation in the lysosome, the latter of which is especially prominent in neural tissue. At least 95% of NPC1 individuals have disease associated variants in the integral membrane-bound NPC1 protein located in the lysosome (NPC1 disease, OMIM #257220). The remaining individuals have pathological variants in the NPC2 protein (NPC2 disease, OMIM #607625), a soluble lysosomal protein that transfers unesterified cholesterol to NPC1 [2]. Clinical presentation of both forms of the disease are similar, where loss of function of NPC1 or NPC2 results in intracellular accumulation of unesterified cholesterol and glycosphingolipids [1, 3-7]. Disease severity and onset is highly variable, affecting infants, children, and adults; however, the classical presentation of NPC1 is most often observed in school-age children and typically includes progressive cerebellar ataxia, vertical supranuclear gaze palsy, gelastic cataplexy, motor deficits, and cognitive impairment as well as visceral manifestations like hepatosplenomegaly [8, 9]. Miglustat, a glycosphingolipid synthesis inhibitor, is approved for treatment for NPC outside the US. Until recently, there were no Food and Drug Administration (FDA) approved therapies for NPC individuals. Then, in September 2024, the FDA approved arimoclomol (Miplyffa, in combination with miglustat) and levacetylleucine (Aqneursa) [10]. Though these and other investigational therapeutics provide some amelioration, all fail to address the root cause of the disorder – the absence of functional NPC1 protein that leads to morbidity and mortality [11-15]. Gene therapy can provide replacement of the dysfunctional NPC1 protein to treat the disease [16, 17].

Many studies have demonstrated that adeno-associated viral (AAV) gene therapy can successfully treat monogenic and rare diseases in pre-clinical models [18-23]. AAVs are already approved for treatment of individuals with disorders such as Spinal Muscular Atrophy (SMA1; onasemnogene abeparvovec-xioi [24-26]), RPE65 mutation associated retinal dystrophy (voretigene neparvovec-rzyl [27, 28]), and aromatic L-amino acid decarboxylase (AADC; eladocagene exuparvovec-tneq [29]). AAV9 is well documented to cross the blood-brain barrier (BBB) and transduce cells of the central nervous system (CNS) [30-34]. Given the devastating neurological impact of NPC1, gene therapy targeting the CNS is imperative. Of note, AAV9 also transduces multiple other organ systems, including the liver and peripheral nerves, that are implicated in NPC1 disease [8, 9, 35-41].

We and others have previously demonstrated that AAV9 vectors can effectively improve survival and delay disease progression in the null $Npc1^{m1N/m1N}$ ($Npc1^{m1N}$, single allele notation for homozygosity) murine model of NPC1 deficiency [18, 42-46]. $Npc1^{m1N}$ mice have a premature stop codon in the *Npc1* gene,

leading to the production of truncated, non-functional NPC1 protein and resulting in a severe disease phenotype [18, 42-51]. Both direct CNS administration (intracerebroventricular or intracisternal magna) [43, 45] and systemic administration (retro-orbital or intracardiac) [18, 42, 44] have successfully ameliorated disease in these mice. Greater success has been noted when using dual routes of CNS administration or administering higher doses of vector to the CNS [45, 46]. We and others have demonstrated that ubiquitous promoters provide greater disease correction in *Npc1*^{m1N} mice as compared to neuron-specific promoters [18, 46]. Further optimization studies have highlighted the therapeutic potential of novel capsids to improve CNS transduction [44].

Many preclinical gene therapy studies in *Npc1*^{m1N} mice have targeted neonates [42, 43, 45, 46]. Previously, we administered AAV9 vectors at 4 weeks old, before onset of phenotypic signs [18, 44]. The question remains whether late(r) intervention can still be effective following diagnoses in individuals after disease onset. Previous clinical studies for aromatic L-amino acid decarboxylase deficiency, a rare pediatric genetic disorder, suggest that AAV gene therapy is universally beneficial but treatment at a younger age was associated with greater benefits [29]. Intervention prior to clinical onset of neurologic symptoms in NPC is currently challenging because NPC1 is not routinely screened for in newborns and the average diagnostic delay remains ~4.1 years [52-55]. However, early intervention prior to neurological onset might be possible in familial cases and after diagnosis when there is infantile presentation with fetal ascites and liver disease [1, 56-58].

More than 600 pathogenic or likely pathogenic NPC1 variants have been described, most of which are missense mutations [59-61]. One of the most prevalent variants is a missense mutation resulting in an amino acid substitution (p.I1061T). The NPC1 p.I1061T protein misfolds and undergoes endoplasmic reticulum associated degradation (ERAD) [62-64]. A knock-in, hypomorphic *Npc1*^{I1061T} allele was generated to recapitulate the human disorder and results in a slightly protracted disease course compared to the more severe *Npc1*^{m1N} mouse model [65]. To assess whether residual NPC1 protein with compromised stability affected gene therapy treatment, we evaluated efficacy of gene therapy in *Npc1*$^{I1061T/I1061T}$ mice (*Npc1*^{I1061T}, single allele notation for homozygosity). We investigated and confirmed that residual NPC1 protein with compromised stability did not interfere with the efficacy of gene therapy.

In this paper we build on our previous work [18, 44], using systemic administration of an AAV9-elongation factor 1α (shortened)-h*NPC1* (AAV9-EF1a(s)-h*NPC1*) vector to treat NPC1 mice. We examine the therapeutic efficacy of this vector across different doses, at timepoints later in disease progression, and in *Npc1*^{I1061T} mice. Our results provide foundational preclinical data for the advancement of AAV9-EF1a(s)-h*NPC1* as a disease modulating therapy for individuals with NPC1 deficiency.

Results:

Dose selection and administration paradigm

Dose selection was based on our previously published work [18, 44], with vector genomes (vg) administered per mouse as the primary parameter. For consistency with other research and clinical trials, doses are also provided in terms of vg/kilogram (vg/kg). The medium dose administered at 4 weeks (1.2×10^{12} vg or 1.28×10^{14} vg/kg) served as the baseline comparator across all studies. Lower and higher doses were chosen to capture a comprehensive dose-response range, considering both experimental and practical constraints which include the vector concentration coupled with our Animal Care and Use Committee's approved volumes for RO delivery. The medium dose was selected for the age at treatment study to ensure sufficient vector was available for full study enrollment.

Npc1^{m1N} mice treated with higher doses of AAV9-EF1a(s)-h*NPC1* show increased survival and delayed disease progression

All mice received a single retro-orbital injection of AAV9-EF1a(s)-h*NPC1* (referred to as AAV9), and each figure panel following includes data from 4-28 mice per group. Regarding statistical analyses, no significant differences between sex were found for any readout measure in the dose, age at treatment, or hypomorphic Npc1 model sub studies. Thus, data from males and females are combined in all statistical tests. The only exception to sex differences is weight curves, which were not analyzed. In this section, mice were sacrificed either at 10 weeks for an age-matched cohort or at humane endpoint for survival.

To compare the efficacy of AAV9 at different doses, mice were injected at 4 weeks old with either low ($1x10^{11}$ vg or $7.87x10^{12}$ vg/kg), medium ($1.2x10^{12}$ vg or $1.28x10^{14}$ vg/kg), or high ($4.3x10^{12}$ vg or $3.06x10^{14}$ vg/kg) dose. A Log-Rank, Mantel Cox test, with Bonferroni's correction for multiple comparisons was used to assess survival (Fig 1A, Table S2A). High- and medium-dose mice had a longer median survival (34.6 and 21.5 weeks, respectively) compared to low-dose (11.4 weeks) and saline-injected mice (10.6 weeks) (for all, $p < 0.0001$). Notably, even the low-dose group had improved survival compared to the saline-injected group (11.4 vs 10.6 weeks, $p = 0.005$).

To determine the effect of AAV9 dose on neurological disease progression, a composite phenotype score was assessed at 3-week intervals from 6 to 18 weeks, where increasing scores indicate disease progression (Fig 1B) [66]. The five neurological phenotypic parameters evaluated for the composite score include hindlimb clasp, motor function, kyphosis, balance, and grooming. High-dose mice showed greatest delay in disease progression, followed by medium dose mice, while low-dose mice mirrored the saline-injected mice (Fig 1B). Two-way ANOVA with mixed effects analysis and Tukey's multiple comparisons test was used to assess differences between groups (Table S3A). Between 6 and 9 weeks, the saline and low-dose groups had similar phenotype scores ($p = 0.95$), while the medium-dose and high-dose groups had significantly lower phenotype scores compared to the saline group (medium-dose: $p = 0.020$, high-dose: $p < 0.0001$) and the low-dose group (medium-dose: $p = 0.007$, high-dose: $p < 0.0001$). Notably, high-dose mice were not significantly different from *Npc1*$^{+/+}$ mice ($p = 0.91$). From 9 to 12 weeks, medium- and high-dose mice continued to show significantly lower phenotype scores than saline-injected and low-dose mice (for all, $p < 0.0001$). High-dose mice maintained lower phenotype scores closer to *Npc1*$^{+/+}$ mice ($p = 0.51$). From 15 to 18 weeks, high-dose mice had significantly lower phenotype scores than medium-dose mice ($p = 0.008$) and did not differ significantly from *Npc1*$^{+/+}$ mice ($p = 0.11$).

Npc1^{m1N} mice exhibit marked weight loss starting at about 6 weeks old. To evaluate disease onset, we assessed the week that mice reached peak weight (Fig 1C) and to evaluate disease progression, we assessed change in weight from 6 to 9 weeks (Fig 1D). Low-dose mice reached peak weight at a similar time to saline-injected mice (6.9 ± 0.6 weeks and 6.8 ± 0.7 weeks, respectively). In contrast, medium dose mice reached peak weight significantly later (11.3 ± 3.9 weeks) than saline-injected ($p = 0.0007$) or low-dose mice ($p = 0.007$). Similarly, high-dose mice reached peak weight significantly later (14.8 ± 3.1 weeks) than saline-injected ($p < 0.0001$) or low-dose mice ($p = 0.0003$). Statistical significance for week of peak weight was determined using a Kruskal-Wallis Test with Dunn's multiple comparisons test. Longitudinal weight data further demonstrates that mice maintain weight and survive longer as the dose of AAV9 increases (Fig S1A, B; Table S4A). When assessing percent weight change from 6 to 9 weeks (Fig 1D), both saline-injected and low-dose mice showed similar percent weight loss (-14.6% ± 6.8% and -9.0% ± 11.7%, respectively; $p = 0.64$) (Fig 1D). In contrast, medium-dose (11.2% ± 13.1%) and high-dose (15.3% ± 10.9%) mice showed significant weight gain compared to both saline-injected and low-dose groups (for all, $p < 0.0001$). Medium-dose and high-dose mice gained weight similarly to *Npc1*$^{+/+}$ mice (5.6% ± 4.1%) during this period (medium-dose: $p = 0.38$, high-dose: $p = 0.15$). Statistical significance for weight change from 6 to 9 weeks was assessed using one-way ANOVA with Tukey's multiple comparisons test.

Higher doses of AAV9 enhance viral transduction in brain and liver of *Npc1*^{m1N} mice

To evaluate the efficacy of vector transduction across tissues, droplet digital PCR (ddPCR) was performed on cerebellar (Fig 2Ai, iii), cerebral (Fig 2Bi, iii) and liver tissues (Fig 2Ci, iii) to assess h*NPC1* copy number at 10 weeks of age or at humane endpoint/survival. In parallel, Western blots were performed to measure NPC1 protein levels present in cerebellum (Fig 2Aii), cerebrum (Fig 2Bii), and liver (Fig 2Cii), as NPC1 protein presence is exclusively attributed to vector transduction in *Npc1*^{m1N} mice.

At 10-weeks-old, high-dose mice exhibited higher h*NPC1* copy numbers in the cerebellum (Fig 2Ai), cerebrum (Fig 2Bi), and liver (Fig 2Ci) compared to all other groups. Similar trends were observed in the spleen, kidney, lung, muscle, and brain stem (Fig S2).

In the cerebellum (Fig 2Aii) and cerebrum (Fig 2Bii), NPC1 protein levels were low, but detectable in high-dose mice and *Npc1*$^{+/+}$ mice, with higher levels observed in *Npc1*$^{+/+}$. In the liver (Fig 2Cii), NPC1 protein was detected only in *Npc1*$^{+/+}$, high-dose, and medium-dose mice, with high-dose mice showing higher average NPC1 protein expression than *Npc1*$^{+/+}$ mice. Representative western blots are shown in Fig S3.

In a linear regression analysis, lifespan was significantly associated with h*NPC1* copy number in the cerebellum and cerebrum within the medium dose group (Fig 2Aiii, Biii). However, two mice with exceptionally high copy numbers in these regions drove significance. In the liver, copy number did not predict lifespan in any individual treatment group (Fig 2Cii, linear regression analysis).

Higher doses of AAV9 reduce cerebellar and hepatic pathology in 10-week-old *Npc1*^{m1N} mice

Cerebellar ataxia is a major clinical feature in NPC individuals and is recapitulated in NPC1 mice with cerebellar pathology and Purkinje neuron degeneration [8, 51, 67]. To assess cholesterol storage and pathological alterations, we performed immunofluorescence staining of the cerebellum in 10-week-old mice. Parallel western blot analysis was used for quantification.

Unesterified cholesterol storage, as visualized by filipin labeling [68], is increased in NPC1 disease [69]. However, high dose gene therapy appears to moderately reduce cholesterol storage compared to other treated or saline-injected mice (Fig 3A). Reactive astrocytosis (GFAP positive staining) is a characteristic finding in both human and mice with NPC1 disease [70-72]. Treatment with AAV9 shows a mild dose-dependent decrease in astrocytosis (Fig 3A). GFAP protein levels do not appear to differ between saline-injected, low-, medium-, or high-dose mice (Fig 3C, representative blot Fig S4A,B).

Progressive loss of Purkinje neurons, particularly from anterior to posterior cerebellar lobules, is a hallmark of NPC1 disease [51, 67] and one with which our data align. Purkinje neuron survival (Calbindin D labeling) appears to improve with increasing doses of AAV9 and correlates with h*NPC1* copy number. Nevertheless, presence of Purkinje neuron remains markedly reduced compared to healthy *Npc1*$^{+/+}$ mice (Fig 3A). A similar dose-dependent increase is observed with Calbindin D protein levels, though levels remain below those of *Npc1*$^{+/+}$ mice (Fig 3D, representative blot Fig S4D,E).

Microglial activation, a well-documented feature of NPC1 pathology [72, 73], appears mildly reduced in high-dose mice, particularly in posterior cerebellar lobules as shown by IBA1 staining (Fig 3B). This reduction is accompanied by a decrease in CD68 protein levels in high-dose mice, a marker of reactive microglia [74] (Fig 3E, representative blot Fig S4B,C).

Hepatomegaly is a common feature of NPC1 disease, with infantile presentation often associated with liver disease [53, 57, 58]. To evaluate liver involvement, we performed immunohistochemical (Fig 4A) and immunofluorescence (Fig 4C) staining of macrophages using CD68 labeling [75] in 10-week-old mice. High- and medium-dose AAV9 treated mice showed a reduced percentage of CD68+ area compared to low-dose and saline-injected mice (Fig 4B, representative images 4A). Additionally, immunofluorescence staining demonstrated a decrease in cholesterol storage (filipin labeling) and macrophage presence (CD68) as the dose of AAV9 increased (Fig 4C).

AAV9 modulates sphingolipid accumulation in the brains of 10-week-old *Npc1^{m1N}* mice

In addition to cholesterol accumulation, multiple lipid classes exhibit altered levels in the NPC1 deficient brain due to impaired NPC1 protein function in mice [76-78]. Among these, gangliosides such as GM2 accumulate in the brains of *Npc1^{m1N}* mice [79]. Mass spectrometry imaging was used to assess the impact of AAV9 dose on sphingolipid distribution in 10-week-old *Npc1^{m1N}* mice and *Npc1$^{+/+}$* mice (Figure S5). While *Npc1$^{+/+}$* mice demonstrated little to no ganglioside accumulation, *Npc1^{m1N}* mice displayed high accumulation in the frontal cortex and cerebellar lobule X. Increasing AAV9 doses led to a qualitative reduction in ganglioside accumulation in both regions (Fig S5Ai). However, quantitative analysis of GM2 (d36:1) levels did not reveal statistically significant differences between groups (Fig S5B).

Beyond gangliosides, sphingolipid distribution is broadly disrupted in *Npc1^{m1N}* mice, with altered distribution of hexosylceramides and dihydroceramides in the cerebellum [80]. Hexosylceramide (HexCer 46:4;O3) levels appeared lower in the cerebellum of *Npc1^{m1N}* mice compared to *Npc1$^{+/+}$* mice. AAV9 treatment was associated with a qualitative increase in HexCer abundance in a dose-dependent manner, particularly in the rostral cerebellar lobules (lobules I-V) (Figure S5BAii). Conversely, dihydroceramide (Cer 32:2;O3) levels appeared elevated in the cerebellum of *Npc1^{m1N}* mice compared to *Npc1$^{+/+}$* mice. While AAV9 had a less pronounced effect on dihydroceramide accumulation, a visual trend towards reduction was observed at medium and high doses (Figure S5Aiii).

AAV9 treatment at 4-weeks improves survival and delays disease progression in *Npc1^{m1N}* compared to treatment at 6- or 8- weeks of age

Npc1^{m1N} mice were treated with 1.28×10^{14} vg/kg of AAV9 at 4 weeks (before onset of neurologic symptoms, hereafter referred to as pre-symptomatic), 6 weeks (early-stage disease), or 8 weeks (late-stage disease) to assess impact of treatment age on therapeutic efficacy. Disease onset is typically observed in *Npc1^{m1N}* mice at 6 weeks, with key manifestations including changes in motor coordination and ataxia that progress until death at approximately 10.6 weeks [66]. For this comparison, mice were sacrificed at 9 weeks to obtain age-matched cohorts or at humane endpoint for survival comparison.

Mice injected at 4 weeks exhibited a significantly longer median survival of 21.5 weeks compared to saline-injected mice (10.6 weeks, $p < 0.0001$) and those treated at 6 weeks (13.2 weeks, $p = 0.003$) or 8 weeks (11.9 weeks, $p < 0.0001$) (Fig 5A). Additionally, mice treated at 6 weeks survived significantly longer than both saline-injected mice ($p < 0.0001$) and mice treated at 8 weeks ($p = 0.0003$), while mice treated at 8 weeks survived longer than saline-injected mice ($p = 0.0006$). Statistical analysis was performed using the Log-Rank Mantel-Cox test with Bonferroni's correction for multiple comparisons, with detailed results provided in Table S2B.

Composite phenotype was assessed between 6 and 18 weeks to evaluate the effect of age of treatment on neurological disease progression (Fig 5B). Between 6 and 9 weeks of age, mice treated at 4 weeks old exhibited significantly lower phenotype scores compared to those at 6 and 8 weeks ($p = 0.001$, $p < 0.0001$

respectively), which progressed similarly ($p = 0.51$). From 9 to 12 weeks, the 4-week group maintained significantly lower composite scores than saline-injected mice ($p < 0.0001$), the 6-week group ($p = 0.0002$), and the 8-week group ($p < 0.0001$), but were higher than *Npc1*$^{+/+}$ mice ($p < 0.0001$). Two-way ANOVA with mixed effects analysis with Tukey's multiple comparisons test were used for statistical analysis, with detailed results presented in Table S3B.

To assess disease onset and progression, we evaluated week of peak weight and percent weight change between 6 and 9 weeks. Mice treated at 4 weeks reached peak weight significantly later (11.3 ± 3.9 weeks) than saline-injected mice (6.8 ± 0.7 weeks, $p = 0.003$) and those treated at 6 weeks (6.8 ± 2.3 weeks, $p < 0.001$) or 8 weeks (6.7 ± 0.6 weeks, $p < 0.001$) (Fig 5C, Kruskal-Wallis with Dunn's multiple comparisons test). In contrast, mice treated at 6 and 8 weeks reached peak weight at similar times as saline-injected mice ($p = 0.82$ and $p > 0.99$, respectively).

When evaluating percent weight change from 6 to 9 weeks, mice injected at 4 weeks (11.2% ± 13.1%) and *Npc1*$^{+/+}$ mice (6.0% ± 4.1%) exhibited weight gain and were significantly different from all other groups ($p < 0.0001$ for all comparisons). In contrast, *Npc1*^{m1N} mice injected at 6 or 8 weeks exhibited weight loss (-12.2% ± 7.7%, -20.0% ± 10.9%, respectively), which was not significantly different from saline-injected *Npc1*^{m1N} mice (-14.6% ± 6.8%; $p = 0.94$, $p = 0.44$, respectively) (Fig 5D, One-way ANOVA with Tukey's multiple comparisons test). Longitudinal weight data further indicate that both male and female cohorts treated earlier maintained weight and survived longer (Fig S2C,D; Table S4B).

Age of treatment affects AAV9 transduction in the cerebellum and treatment at 4 weeks reduces cerebellar pathology in 9-week-old *Npc1*^{m1N} mice

h*NPC1* copy number in the cerebellum was assessed in 9-week-old mice. Mice injected at 4 and 6 weeks had higher h*NPC1* copy numbers than saline mice or mice injected at 8 weeks (Fig 6A). NPC1 protein levels were similar across all treated mice (Fig 6B, representative blot Fig S6A,B).

Immunofluorescence staining and Western blots were utilized to evaluate cerebellar pathology in age-matched mice. Mice treated at 4 weeks demonstrated greater Purkinje neuron survival in anterior lobules and the entire cerebellum when compared to saline-injected mice and those treated at 6 or 8 weeks (Fig 6C); this pattern is also consistent with increased Calbindin D protein levels in mice treated at 4 weeks (Fig 6E, representative blot Fig S6A,B). Further, microgliosis appears mildly reduced in the posterior lobules of the cerebellum in the 4-week group compared to saline-injected and other treated mice (IBA1 labeling, Fig 6D). A similar reduction was observed in CD68 protein levels in the 4-week group, indicating decreased reactive microglial activity (Fig 6F, representative blot Fig S6C,D). Finally, GFAP protein levels (reactive astrocytosis) appear similar across all groups (Fig 6G, representative blot Fig S6C,D).

Age of treatment impacts AAV9 transduction in cerebrum and liver of *Npc1*^{m1N} mice

h*NPC1* copy number in the cerebrum and liver was also assessed via ddPCR in the age-matched cohort (9 weeks) and at humane endpoint. In the age-matched cohort, mice injected at 8 weeks exhibited the highest h*NPC1* copy number in the cerebrum compared to all other groups (Fig 7A). In the cerebrum, high copy numbers in 4- and 6-week-old injected groups were associated with longer lifespans based on linear regression analysis; however, two mice with exceptionally high copy numbers in the 4-week group drive significance in this finding. In mice treated at 8 weeks, copy number did not predict lifespan (Fig 7B).

In the livers of the age-matched cohort, mice treated at 8 weeks again had higher h*NPC1* copy numbers than other treated and saline-injected mice (Fig 7C). Linear regression analysis shows that higher copy

346 numbers in the liver predicted lifespan only in mice treated at 6-weeks old (Fig 7D). In mice from the age-
347 matched cohort, immunohistochemical staining revealed a reduced presence of CD68+ macrophages in the
348 liver of mice treated at 6 weeks compared to other treated and saline-injected mice (Fig 7F; representative
349 images Fig 7E).
350
351
352 **$Npc1^{I1061T}$ mice treated with AAV9 show improved lifespan and delayed disease progression**
353
354 To evaluate efficacy of AAV9 in a hypomorphic mouse model of NPC1 deficiency, $Npc1^{I1061T}$ mice were
355 treated with 1.28×10^{14} vg/kg (1.2×10^{12} vg per mouse) of AAV9 at 4 weeks old. In this sub study, mice were
356 sacrificed at 14 weeks for an age-matched cohort or humane endpoint for survival.
357
358 AAV9 treated $Npc1^{I1061T}$ mice had a median survival of 22.9 weeks, significantly longer than the 15.0 weeks
359 observed in saline-injected mice (Fig 8A, Log-Rank Mantel-Cox test, $p < 0.0001$). Previous studies report
360 a median survival of about 17.9 weeks for $Npc1^{I1061T}$ mice, while $Npc1^{m1N}$ mice typically survive to 10.5
361 weeks [65], and phenotypic onset in $Npc1^{I1061T}$ mice occurs at 9-10 weeks; assessments were adjusted
362 accordingly to account for differences in lifespan compared to the $Npc1^{m1N}$ model.
363
364 Disease phenotype was also evaluated in treated and untreated mice to determine efficacy of gene therapy
365 in slowing progression (Fig 8B). From weeks 9-12 and weeks 12-15, AAV9 treated $Npc1^{I1061T}$ mice had
366 significantly lower composite scores compared to saline-injected mice, but scores were still higher than
367 $Npc1^{+/+}$ mice ($p < 0.0001$ for all comparisons; two-way ANOVA with mixed effects analysis with Tukey's
368 multiple comparisons test).
369
370 Week of peak weight and percent weight change between 10 and 14 weeks were evaluated to assess disease
371 onset and progression. Treated mice reached peak weight significantly later than saline-injected mice (12.9
372 ± 3.8 weeks vs. 10.9 ± 1.1 weeks; $p = 0.008$, Mann-Whitney test) (Fig 8C). Treated mice gained weight
373 from 10-14 weeks (3.8% ± 6.0%), similar to $Npc1^{+/+}$ mice (7.3% ± 2.7%) ($p = 0.37$). In contrast, saline-
374 injected mice lost weight (-12.3% ± 11.0%) and were significantly different from treated ($p = 0.01$) mice
375 (Fig 8D, Kruskal-Wallis test with Dunn's multiple comparisons test). Longitudinal weight data further
376 demonstrates that treated mice survive and maintain weight longer than saline-injected $Npc1^{I1061T}$ mice (Fig
377 S1E,F; Table S4C).
378
379 **AAV9 treatment transduces the cerebellum of $Npc1^{I1061T}$ mice but without pathological**
380 **improvement**
381
382 ddPCR was used to assess h*NPC1* copy number in the cerebellum of mice at 14-weeks old (age-matched
383 cohort). At 14 weeks, the typical end stage for untreated $Npc1^{I1061T}$ mice, treated mice demonstrated
384 increased h*NPC1* copy numbers compared to saline-injected mice ($p = 0.008$, Kruskal-Wallis test with
385 Dunn's multiple comparisons test; Fig 9A). Parallel western blot analysis confirmed similar NPC1 protein
386 presence in treated and saline-injected $Npc1^{I1061T}$ mice (NPC1 protein antibody captures both human and
387 mouse NPC1) (Fig 9B, representative blot in Fig S7A,B).
388
389 Cerebellar pathology in the age-matched cohort was evaluated using immunofluorescence staining and
390 western blotting. $Npc1^{I1061T}$ mice treated with AAV9 showed some survival of Purkinje neurons in anterior
391 lobules of the cerebellum. However, global Purkinje neuron loss across the cerebellum remained
392 comparable between treated and saline-injected mice (Fig 9C). Analysis of Calbindin D protein levels
393 revealed similarly low Calbindin D levels in the cerebellum of treated and saline-injected mice, both of
394 which were lower than healthy $Npc1^{+/+}$ mice (Fig 9E, representative blot Fig S7C,D). Microgliosis did not
395 appear reduced in treated mice compared to saline-injected mice, as indicated by IBA1 labeling (Fig 9D).

Similarly, CD68 protein levels, a reactive microglial marker, do not appear reduced in the cerebellum of treated mice (Fig 9F, representative blot Fig S7E,F). Finally, reactive astrocytosis, as measured by GFAP protein levels, is similar in treated mice compared to saline-injected mice (Fig 9G, representative blot Fig S7G,H).

AAV9 treatment of *Npc1*^{I1061T} mice results in successful transduction of cerebrum and liver with reduced hepatic pathology

ddPCR was used to measure h*NPC1* copy number in the cerebrum and liver in the age-matched cohort (14-weeks old) and at humane endpoint/survival. In the age-matched cohort, h*NPC1* copy number in both the cerebrum (Fig 10A) and liver (Fig 10C) were elevated compared to saline-injected mice. In the cerebrum, an increasing h*NPC1* copy number significantly predicted extended lifespan (Fig 10B), whereas in the liver, an increase in h*NPC1* copy number was significantly associated with decreased lifespan (Fig 10D) (linear regression analysis). In the liver of age-matched mice, immunohistochemical staining revealed a partial reduction of CD68+ macrophages compared to saline-injected mice, albeit not to normal *Npc1*$^{+/+}$ levels (Fig 10F; representative images Fig 10E).

Discussion

We examined dose and age at intervention as key factors in optimizing systemically delivered AAV9-EF1a(s)-h*NPC1* gene therapy. Higher doses of AAV9-EF1a(s)-h*NPC1* and treatment during the pre-symptomatic period in the null *Npc1*^{m1N} model significantly improved survival and slowed disease progression compared to lower doses or later treatment. Notably, mice receiving higher doses had the longest survival times, though they did ultimately succumb to NPC1 disease. Additionally, we assessed efficacy of gene therapy in the hypomorphic *Npc1*^{I1061T} mouse, which carries a missense variant, and found that AAV9-EF1a(s)-h*NPC1* successfully increased survival and slowed disease progression in this model.

NPC1 can manifest early and severely, though many individuals experience the first neurological sign in childhood or adolescence, often followed by significant diagnostic delays. Previous gene therapy studies have focused on treatment of neonatal *Npc1*^{m1N} mice [42, 43, 45, 46]. Importantly, we assessed gene therapy efficacy in juvenile mice before and after symptom onset. *Npc1*^{m1N} mice treated pre-symptomatically showed greatest improvements in survival and slowed disease progression. However, mice treated in early disease stage (6 weeks) still exhibited slight survival benefits, indicating the value of early-symptomatic treatment. Establishing a dose- and age-dependent effect is crucial, especially for diseases like NPC1, which are typically diagnosed symptomatically and are not currently part of newborn screening. By demonstrating the benefits of early intervention, our work highlights the need for expanded newborn screening programs, which would enable earlier diagnosis and support treatment of NPC1 individuals before neurological manifestations occur.

Although the *Npc1*^{I1061T} model has not been previously studied, another hypomorphic mouse model (*Npc1*^{nmf164}) which carries a D1005G amino acid substitution, has been examined in gene therapy studies [46]. Both models exhibit late-onset and slower progression compared to *Npc1*^{m1N} mice, which more closely mirrors most human cases. However, the D1005G residue is not conserved in humans and its impact on protein folding or stability is unclear [81]. In contrast, the *Npc1*^{I1061T} model represents a prevalent human variant, with NPC1 p.I1061T encoding a misfolded protein targeted for ERAD [64, 65]. This variant is the most common disease-causing allele in individuals of European descent, accounting for 15-20% of pathological alleles [62, 82, 83]. We demonstrate significant improvement in survival, delayed disease progression, and liver (though not cerebellar) pathology with systemic gene therapy, even in the presence

445 of residual NPC1 protein. These findings might suggest broader applicability of gene therapy across
446 different patient populations, including those with slower-progressing, later-onset NPC1.
447
448 While our high dose showed the most significant survival benefits and improved transduction of multiple
449 organs affected by NPC1, its direct translation to humans requires careful consideration. For comparison,
450 Zolgensma, an FDA-approved therapy for SMA1, is administered at $1.1x10^{14}$ vg/kg, whereas our high dose
451 of $3.06x10^{14}$ vg/kg exceeds that level. Although we did not observe toxicity at this higher dose, clinical
452 experiences with AAV8-mediated gene therapy for X-linked myotubular myopathy underscore potential
453 risks, where 3 of 14 patients experienced fatal liver failure at a dose of $3.5x10^{14}$ vg/kg [84]. These
454 observations highlight the importance of dose escalation studies in preclinical models to refine dosing
455 strategies for translation to human applications. Our medium AAV9 dose of $1.28x10^{14}$ vg/kg – comparable
456 to Zolgensma – showed significant improvements in survival and disease progression, suggesting that doses
457 within this range could balance efficacy and safety. Mice receiving higher doses had the longest survival
458 times, though they ultimately succumbed to disease progression. As necropsies were not carried out, the
459 exact cause of death at the predefined humane endpoint is not known. We hypothesize that because many
460 neurons and cells throughout the CNS remain uncorrected following a single injection of the gene therapy,
461 the disease burden eventually outweighs the capabilities of the transduced, healthy cells. If correct, this
462 theory highlights the importance of widespread transduction, best case scenario being correction of 100%
463 of cells, especially of neurons throughout the CNS. Recognizing this is not yet possible, toxicity must be
464 assessed for high doses aimed at maximizing transduction prior to clinical translation. Together, these
465 findings support the notion that increasing doses achieve greater benefit, the importance of achieving
466 adequate dosing for therapeutic efficacy, and the need to balance efficacy with safety in future studies.
467
468 Regarding readout measures of mice in the same dose group, a comparison of weight metrics reveals greater
469 variability in the medium and high dose treatment groups while survival in the medium dose group covers
470 a wide range. Retro-orbital administration, as performed by human hand, is subject to inconsistency. To
471 minimize this potential confounder, a veterinarian with extensive surgical experience in rodent models was
472 the only person to perform RO injections for gene therapy studies from our group to date. Another potential
473 contributor to variability within the different readout measures is weight at time of injection. However, no
474 significant correlation was found between this data metric and the survival, h*NPC1* copy number, or percent
475 weight gain from 6-9 weeks of age. Finally, handling of vector and different vector productions could
476 contribute to variability. To minimize this risk, all vector productions were purchased from University of
477 Pennsylvania Vector Core, now Franklin Biolabs. Vector was thawed only once following dilution and the
478 same vector production batch was used for the high and low dose cohorts. The medium dose cohort/study
479 spanned a greater range of time and provided an internal control as three different batches were used. There
480 was no correlation between the vector batch and lifespan of the mice in the medium dose cohort.
481
482 To compare the effects of age of treatment in $Npc1^{m1N}$ mice, we used a fixed-analysis point at 9 weeks of
483 age, just before humane endpoint. This age-matched timepoint allowed for consistent comparisons of
484 pathology and vector transduction but did not account for treatment-duration-matched intervals (e.g.,
485 assessing all mice at a fixed period, such as 2 weeks post-treatment). Notably, mice treated at 8 weeks
486 exhibited higher h*NPC1* copy numbers in the cerebrum and liver compared to those treated at 4 or 6 weeks.
487 However, it is unclear if this trend would persist in a treatment-duration-matched cohort. Future studies
488 could explore post-treatment intervals to better understand how vector expression changes over time and
489 more directly compare the impact of age of treatment on transduction efficiency.
490
491 Additionally, we did not determine which cell types were transduced by AAV9 administration or whether
492 neuronal dysfunction or loss contributed more to pathology. Future studies might assess the transduction of
493 cell types across the brain, investigating both cell death and dysfunction. For instance, we observed Purkinje
494 neuron loss in the cerebellum (a well-described phenomenon [67]), but others have described lipid storage
495 without cell loss in the pyramidal cells of the hippocampus [85, 86]. Understanding which cell types are

496 most affected and best transduced is essential for clinical success of this gene therapy. Another limitation
497 of this study is the absence of direct quantification of accumulating metabolites in the brain. For example,
498 while the overall cholesterol levels in the brain remain unchanged in NPC1, its intracellular localization is
499 disrupted, leading to pathological effects [8, 87]. To address lipid accumulation, we used mass spectrometry
500 imaging to measure changes in sphingolipids that change in both quantity and distribution. This provided
501 valuable insights into lipid changes in response to treatment, but future studies could incorporate high-
502 performance liquid chromatography to enhance our understanding of lipid storage correction after gene
503 therapy by broadening the analysis of lipid metabolites.
504
505 Future studies could also explore combining NPC1 gene therapy with chaperone molecules or substrate
506 reduction therapy, given that gene therapy alone does not entirely halt disease progression. For example,
507 Miglustat, an FDA-designated compound for use in combination with arimoclomol (Miplyffa), reduces
508 glycosphingolipid accumulation but does not address the root cause [10, 88, 89]. Incorporating gene therapy
509 could address this root cause while enhancing therapeutic outcomes by simultaneously reducing disease
510 burden.
511
512 In summary, systemic AAV9-EF1a(s)-h*NPC1* delivery significantly impacts NPC1 disease phenotypes and
513 improves survival in both severe and milder disease models, with delivery of high doses and pre-
514 symptomatic treatment providing greatest impact. The findings presented here lay the groundwork for
515 translating this promising therapy to clinical trials for individuals with NPC1 deficiency. Our work has
516 broader implications for gene therapy targeting other lysosomal-membrane spanning proteins, such as those
517 implicated in neuronal ceroid lipofuscinosis [20, 90, 91] and Mucolipidosis type IV [92, 93]. The ability of
518 gene therapy to improve survival and delay disease progression in juvenile mice offers hope for diseases
519 where early detection and intervention remain significant challenges. While gene therapy may not entirely
520 halt disease progression in NPC1, the demonstrated survival benefits emphasize its potential in managing
521 other similar disorders where early, aggressive intervention is critical.
522

523 # Materials & Methods

524

525 **Vector construction and production**

526 The vector, AAV9-EF1a(s)-h*NPC1* was previously described and produced by the University of
527 Pennsylvania Vector Core [18].
528

529 **Animals**

530 All animal work in these studies was carried out in accordance with the National Institutes of Health Animal
531 Care and Use Committee approved protocols. Heterozygous (BALB/cNctr-$Npc1^{m1N}$/J strain; Jackson
532 Laboratory strain # 003092) $Npc1^{+/m1N}$ mice were crossed to obtain homozygous mutants ($Npc1^{m1N/m1N}$) and
533 wildtype controls ($Npc1^{+/+}$). $Npc1^{I1061T}$ mice were generated by crossing heterozygous $Npc1^{+/I1061T}$ mice
534 (B6.129-$Npc1^{tm1Dso}$/J strain; Jackson Laboratory strain # 027704) to obtain homozygous mutants and
535 $Npc1^{+/+}$ controls. We use single allele notation to indicate homozygosity. Mice were weighed weekly and
536 then more frequently as the disease progression neared humane endpoint. Mice were euthanized at a
537 predefined humane endpoint which occurred when at least two of the following four criteria were met:
538 weight falling below 70% of peak weight, repeatedly falling to side during movement, dull eyes or palpebral
539 closure of eyes, or reluctance to move.
540

541 As per the ARRIVE Essential 10, the following information refers to the studies contained herein. All
542 studies included saline-injected or untreated mice ($Npc1^{m1N}$ or $Npc1^{+/+}$, respectively) as control groups. The
543 same control mice from the $Npc1^{m1N}$ line were used for the dose and age at injection studies while an
544 appropriate groups of control mice from the $Npc1^{I1061T}$ line were used for the corresponding study. A total
545 of 238 mice were used in these studies. Group sample size is stated in the legend or figure for each analysis.

Data for dose and age of treatment study includes all saline-injected and medium-dose AAV9 *Npc1*^{m1N} mice as well as untreated *Npc1*$^{+/+}$ at 4 weeks. No specific exclusion criteria were set a priori, and all mice included in the studies were randomly assigned to treatment or control groups using a blocking method. Except for the researcher overseeing the studies, those involved in vector injections and data acquisition remained blinded to the greatest extent possible. The primary outcome measure was survival. Secondary outcome measures included behavioral assessments, weight, h*NPC1* copy number, and pathology. Details of statistical analyses are found in the results, methods, or figure legends. Experimental animals, procedures, and results are contained with the methods and results of this publication.

Phenotypic Assessment

Mice were tested starting at 6 weeks of age (phenotypic onset) and every three weeks thereafter until humane endpoint or inability to complete the evaluation. The phenotype score evaluates five behaviors associated with the NPC1 phenotype in diseased mice as previously described: hindlimb clasp, motor function, kyphosis, grooming, and a balance-ledge test for cerebellar ataxia [66]. Each phenotype is scored from 0 to 3 with increasing scores representing a more compromised disease state.

Phenotypic testing was carried out in a blinded fashion such that individual mice within a cage had distinct tail markings. Evaluators had access only to cage card numbers and tail markings to identify mice. The order in which mice were tested varied for each testing date. All animals were group housed.

Administration of vector

Treated *Npc1*^{m1N} mice received a retro-orbital injection of AAV9-EF1a(s)-h*NPC1* at 4 weeks (weaning), 6 weeks, or 8 weeks of age. *Npc1*^{I1061T} mice received a retro-orbital injection of AAV9-EF1a(s)-h*NPC1* at 4 weeks old. Control littermate *Npc1*^{m1N} or *Npc1*^{I1061T} mice received a retro-orbital injection of 0.9% saline at 4 weeks or the specified age. Mice were anesthetized using isoflurane for 30-60s and then injected retro-orbitally with a 30-gauge needle affixed to a 0.3 cc syringe. Some control *Npc1*$^{+/+}$ mice received retro-orbital injections of saline while others remained un-injected.

Dose Selection

Our original dose for mice treated at 4 weeks was 1.2×10^{12} vector genomes (vg) per mouse (mean: 1.28×10^{14} vg/kg), based on our previously published data [18, 44]. This served as the medium dose and the comparator across studies. For ease of comparison to other animal and clinical studies, doses are provided as vector genomes/kg.

For dose comparison, doses were selected and scaled based on vector genomes/mouse. We used a low dose of 1×10^{11} vg/mouse (7.87×10^{12} vg/kg), representing a 1-log reduction from the baseline. The high dose, 4.3×10^{12} vg/mouse (3.06×10^{14} vg/kg), was dictated by the maximum concentration achievable through the University of Pennsylvania Vector Core, now Franklin Biolabs, and volume constraints allowed by the Animal Care and Use Committee. For the age of treatment study, dose was calculated per weight to deliver 1.28×10^{14} vg/kg for each mouse at either 6 or 8 weeks of age.

Tissue collection and homogenization

Mice were anesthetized with an intraperitoneal injection of Avertin (lethal dose of 0.04 mL/gm) for euthanasia as previously described [44]. When mice were insensate, the chest cavity was opened, and mice were perfused with 0.9% saline. Immediately, half of the brain, one lobe of the liver, and a piece of spleen, kidney, lung, and leg muscle were collected and frozen on dry ice for tissue homogenization. Mice were then perfused again with 4% paraformaldehyde to fix tissues; remaining organs (half of the brain, liver) were collected and stored post-fixation in 4% PFA overnight and then rinsed and stored in phosphate-buffered-saline (PBS).

596 A Benchmark Scientific Beadbug homogenizer was used to homogenize frozen tissue with UltraPure water.
597 Tissue was placed in tubes with 3 mm zirconium beads (cerebrum, cerebellum, brainstem, liver, spleen, leg
598 muscle) or 1.5 mm zirconium beads (kidney, lung) and homogenized 3 times for 30 seconds at speed 400.
599 Resulting homogenate was aliquoted into tubes for DNA extraction and protein analysis, the latter of which
600 also had RIPA buffer with proteinase inhibitor cocktail (11 836 170 001; Millipore Sigma, Burlington, MA)
601 [44].
602
603 **Western blotting**
604 Protein levels from cerebrum, cerebellum, and liver homogenates were quantified using a BCA Assay
605 (23225, Thermo Fisher Scientific, Waltham, MA). Equal amounts of protein (50 ug for liver, cerebellum,
606 and cerebrum) were run on 4-12% Bis-Tris SDS-polyacrylamide gels (NP0321BOX/Invitrogen by Thermo
607 Fisher Scientific) and separation was achieved via electrophoresis; protein was then transferred to a
608 nitrocellulose membrane (Life Technologies) and blocked for 1 hour in 5% milk in 0.01% PBSTween.
609 Samples were washed in 0.01% PBSTween incubated overnight at 4 °C on a rocking platform with primary
610 antibody (Table S1). Blots were washed three times and incubated with secondary antibodies for 1 hour at
611 room temperature (Table S1), then washed again. Bands were imaged using the LI-COR Odyssey® CLx
612 Imaging System.
613
614 **Histology**
615 Brain and liver tissue from each group were acquired at 9 or 10 weeks of age (*Npc1*^{m1N}), 14 weeks of age
616 (*Npc1*^{I1061T}), or humane endpoint (both models). Post-fixation tissues were embedded in agarose blocks
617 (3.5% agarose, 8% sucrose, PBS) and sectioned parasagittaly (30 µm) using a Leica VT1200 S vibratome.
618 Free-floating sections were collected, incubated in 1.6% H_2O_2 in PBS, then washed in 0.25% Triton X-
619 100/PBS (PBSt). After blocking for 1 hour at room temperature in PBSt/normal goat serum, samples were
620 incubated in primary antibodies overnight at 4°C (Table S1). Samples were washed in PBSt and then
621 incubated with secondary antibodies for 1 hour at room temperature (AlexaFluor 488 or 594; Table S1).
622 Filipin staining (Sigma-Aldrich, F9765) was finally performed to allow visualization of unesterified
623 cholesterol accumulation (0.05mg/mL) with a 20-minute incubation. ProLong Gold mounting medium
624 alone (Thermo Fisher Scientific, P36934) or with DAPI (Thermo Fisher Scientific, P36935) was used to
625 coverslip after mounting tissue sections to slides.
626
627 For immunohistochemical staining after primary antibody incubation, slides were incubated in biotinylated
628 secondary antibody and washed in PBSt. A biotinylated horse radish peroxidase was preincubated with
629 avidin to form Avidin-Biotin Complex (ABC; Vector Laboratories SK-4100) and the tissues were incubated
630 in ABC (in PBS) for 1 hour. Tissues were then washed in PBS and incubated for 10 minutes in a 3,3'-
631 Diaminobenzidine (DAB; Vector Laboratories PK-4000) solution before mounting and cover slipping with
632 VectaMount (Vector Laboratories, H-5700).
633
634 Histoserv, Inc. (Germantown, MD) performed paraffin embedding (formalin fixed, paraffin embedded i.e.,
635 FFPE, tissues). For immunofluorescent staining, FFPE sections (3 um) were collected and underwent
636 antigen retrieval in a citrate (pH 6.0, Electron Microscopy Sciences, 62706-10) or Tris-EDTA (pH 9.0,
637 Abcam, AB93684) buffer. Slides were then incubated in primary antibody diluted in antibody diluent with
638 BSA and preservative (Thermo Fisher Scientific, 003218) at 37°C for 1 hour, washed in PBS, and incubated
639 in secondary antibodies for 30 minutes at 37°C (Table S1). Tissues were then coverslipped with ProLong
640 Gold mounting medium with DAPI.
641
642 **Image capture and analysis**
643 Fluorescent imaging was performed with an inverted Zeiss AxioScan Z1slide scanner with Zen Blue 3.8 as
644 previously described in [44]. Brightfield images were captured on the same Zeiss AxioScan Z1 slide
645 scanner. Adobe Photoshop 2023 (v.23.5.0) and 2024 (v.25.1.0) was used to modify all images in a
646 figure/group identically by resizing and adjusting brightness and/or contrast.

Quantification of CD68 area

Percent of positive CD68 area relative to total area in liver sections was determined according to methods previously described [94] using Image-Pro. V11 software (Media Cybernetics, Inc.). Images were processed using ten regions of interest with total area 900,000 μm^2 to determine average percent positive area.

Copy number analysis by ddPCR

Vector copy number was measured by droplet digital PCR (ddPCR) as previously described with h*NPC1* and *GAPDH* primers (Bio-Rad; [44]). 0.5-50 ng of DNA was used for gene copy number quantification with brain (cerebrum, cerebellum, or brainstem) and liver homogenates. Additional organs including spleen, kidney, lung, and leg muscle were assayed for the 10-week-old cohort in the dose study, using 0.5-5 ng of DNA per reaction. Signals for droplets were either positive or negative for h*NPC1* and/or *GAPDH* as determined using BioRad's QuantaSoft version 1.7.4.0917 software.

Mass spectrometry imaging and lipidomics

The fresh frozen half of the brain was sectioned on a CryoStar NX50 Cryostat set to -12°C in preparation for mass spectrometry imaging. The frozen tissue was divided into 4-6 10 µm thick sections, which were then promptly thaw-mounted onto ITO slides (MIDSCI) and stored at -80°C. Immediately prior to imaging sections, the slides were removed from the -80°C freezer and washed with ice cold 50 mM ammonium formate for 20 seconds then dried in vacuo. 9-aminoacridine and 2,5-dihydroxybenzoic acid were chosen as the matrices for negative and positive mode respectively. One hundred milligrams of solid matrix was dissolved in 10 mL of 50:50 H_2O:ACN + 0.2% TFA and filtered using a 0.2 µm syringe filter. Filtered matrix was applied to the slide using the HTX TM Sprayer.

Mass spectrometry imaging was performed on a Bruker RapifleX MALDI TOF with a 10 kHz laser set to 60% power, 500 laser shots per pixel, and a step size of 35 µm. The instrument was operated in negative and positive mode within an m/z range of 200-1800. All data processing including region-of-interest determination, spatial segmentation, mass spectra extraction and image generation were performed using Bruker's Scils software. LIPID MAPS and the Human Metabolome Database were used to annotate and identify lipids according to accurate mass measurements. Hedges-g analysis was performed for GM2 lipid species across the experimental groups using total ion count normalized peak areas.

Statistical analysis

Randomization was achieved with multiple cohorts. Mice within each cohort were included from each age at injection group or at each dosage. Statistical analysis was performed using GraphPad Prism version 9.5.1 for Windows or Mac. Normality was evaluated for data sets and appropriate parametric or nonparametric tests were selected for further analysis. Data is presented as mean ± SD. Kaplan Meier survival curves used Log-Rank Mantel-Cox test to assess significance, with a Bonferroni-correction applied for $P<0.0083$ for multiple (six) comparisons. Other statistical tests were as follows: Kruskal-Wallis test with Dunn's multiple comparison's test, one-way ANOVA with Tukey's multiple comparisons test, two-way ANOVA with Tukey's multiple comparisons test, linear regression test (all multiple comparisons test use post hoc Bonferroni's correction). In all figures: * $p < 0.05$, ** $p < 0.01$, *** $p < 0.001$, **** $p < 0.0001$.

Acknowledgments:

We thank Laura L. Baxter for her support and instruction in statistical analysis as well as Stephen Wincovitch for imaging and quantification support. We are grateful for the technical assistance in digital droplet PCR provided by the National Cancer Institute Genomics Core. We sincerely acknowledge the NIH animal care and veterinary staff for the care of mice used in these studies. We also recognize the driving

696 force behind this work: individuals with NPC1 disease. Their perseverance in the face of this debilitating
697 disease inspires and humbles us.

698 **Funding**

699 This work was supported by the Intramural Research Program of the National Human Genome Research
700 Institute (NHGRI) at the NIH (1ZIAHG000068-16), the *Eunice Kennedy Schriver* National Institute of
701 Child Health and Human Development (NICHD) at the NIH (ZIAHD008988), grants from the NIH
702 (R01NS114413, R01NS124784), and the Ara Parseghian Medical Research Fund at the University of Notre
703 Dame. AVM, ALG, TG, CDD, AI, CPV, and WJP were supported by the Intramural Research Program at
704 NHGRI; CDD, KM, SRG, FDP were supported by the Intramural Research Program at NICHD. Additional
705 support for CDD came from the Support Of Accelerated Research for NPC (Hide & Seek Foundation and
706 Dana's Angels Research Trust). DP-J was supported by the Bridge to Doctoral Program and the
707 Diversifying Faculty in Illinois Fellowship.

708 Conflict of Interest Statement

709 CPV and WJP have NIH patents filed on work related to NPC1 genes and the AAV gene therapy treatment
710 of NPC1 (US Patent Publication Numbers 20180104289, 20210113635).

711

712 **Figure 1: *Npc1^{m1N}* mice treated with AAV9-EF1a(s)-h*NPC1* vector show increased survival and**
713 **delayed disease phenotype progression.**
714 **(A)** Kaplan-Meier survival curve of mice treated with low, medium, and high dose AAV9 and saline
715 injected mice (results presented in Table S2A) (saline n = 15, low n = 10, medium n = 24, high n =8). **(B)**
716 Composite phenotype scores for each dosage group with measurements taken every 3 weeks, starting at 6
717 weeks (results presented in Table S3A) (saline n = 14, low n = 10, medium n = 13, high n = 8, *Npc1*$^{+/+}$ n =
718 21). **(C)** Week at which mice reached peak weight (Kruskal-Wallis with Dunn's multiple comparisons test).
719 **(D)** Percent weight change between 6 and 9 weeks old (One-way ANOVA with Tukey's multiple
720 comparisons test). For (C, D): saline n =15, low n = 10, medium n = 24, high n = 8; for (D): *Npc1*$^{+/+}$ n =
721 21. For all: * $p < 0.05$, ** $p < 0.01$, *** $p < 0.001$, **** $p < 0.0001$. Data presented as mean ± SD for B,
722 C, D.
723

724 **Figure 2: Higher dose of AAV9 enhance viral transduction in brain and liver of *Npc1^{m1N}* mice.**
725 **(A, B, C)** Analysis of cerebellum (A), cerebrum (B), and liver (C). **(Ai, Bi, Ci)** h*NPC1* copy number in
726 cerebellum (Ai), cerebrum (Bi), and liver (Ci) from 10-week-old mice (Kruskal-Wallis test with Dunn's
727 multiple comparisons test). For Ai, Bi, Ci: (saline n = 6, low n = 5, medium n = 6, high n = 6, *Npc1*$^{+/+}$ n =
728 9). **(Aii, Bii, Cii)** NPC1 protein levels were assessed via western blot in 10-week-old mice to confirm
729 amount of NPC1 protein in the cerebellum (Aii), cerebrum (Bii) and liver (Cii) (Kruskal-Wallis test with
730 Dunn's multiple comparisons test). For Aii (saline n = 6, low n = 5, medium n = 6, high n = 6, *Npc1*$^{+/+}$ n =
731 8). For Bii, Cii (saline n = 6, low n = 5, medium n = 6, high n = 6, *Npc1*$^{+/+}$ n = 7). **(Aiii, Biii, Ciii)** Linear
732 regression of h*NPC1* copy number in the cerebellum (Aii), cerebrum (Bii) and liver (Cii) in end stage mice.
733 For Aiii, Biii (saline n = 14, low n = 9, medium n = 20, high n = 6, *Npc1*$^{+/+}$ n = 17). For Ciii (saline n = 14,
734 low n = 9, medium n = 18, high n = 5, *Npc1*$^{+/+}$ n = 17). For all: * $p < 0.05$, ** $p < 0.01$, *** $p < 0.001$, ****
735 $p < 0.0001$. Data presented as mean ± SD for Ai, Bi, Ci, Aii, Bii, Cii.
736

737 **Figure 3: Dose-dependent amelioration of cerebellar pathology in 10-week-old *Npc1^{m1N}* mice.**
738 **(A)** Representative immunofluorescence staining in free floating sections for: unesterified cholesterol
739 storage (top row), reactive astrocytes and Bergmann glia (middle row), and Purkinje neurons (bottom row).
740 Insets are of anterior lobules (IV/V). **(B)** Representative immunofluorescence staining in formalin-fixed,
741 paraffin embedded sections for microgliosis. Insets are of posterior lobules (lobule IX). For (A, B) Scale
742 bar = 1000 microns for panels, 250 microns for insets. **(C, D, E)** Protein levels for GFAP (C), Calbindin
743 (D), CD68 (E), were assessed via western blot for 10-week-old mice (Kruskal-Wallis test with Dunn's
744 multiple comparisons test) (saline n = 5, low n = 5, medium n = 6, high n = 5, *Npc1*$^{+/+}$ n = 5). For C, D, E:
745 * $p < 0.05$, ** $p < 0.01$, *** $p < 0.001$, **** $p < 0.0001$, data presented as mean ± SD.
746

747 **Figure 4: Dose-dependent reduction of liver pathology in 10-week-old *Npc1^{m1N}* mice.**
748 **(A)** Representative CD68+ immunohistochemical staining of macrophages (free floating sections). Scale
749 bar = 250 microns. **(B)** Quantification of percent area CD68 labelled in 10-week-old mice (Kruskal-Wallis
750 test with Dunn's multiple comparisons test) (saline n = 5, low n = 5, medium n = 6, high n = 6, *Npc1*$^{+/+}$ n
751 = 9). **(C)** Representative cholesterol storage (filipin labeling) and CD68+ immunofluorescent staining in
752 the liver (free floating sections). Yellow arrows in high-dose inset denote groups of cells without cholesterol
753 storage. Scale bar for panel (A) = 500 microns, scale bar for (C) = 100 microns. For B: * $p < 0.05$, ** $p <$
754 0.01, *** $p < 0.001$, **** $p < 0.0001$, data presented as mean ± SD.
755

756 **Figure 5: AAV9 treatment at 4-weeks improves survival and delays disease progression in *Npc1^{m1N}***
757 **compared to treatment at 6- or 8- weeks of age.**
758 **(A)** Kaplan-Meier survival curve of mice treated with AAV9 (results presented in Table S2B). **(B)**
759 Composite phenotype scores for each dosage group with measurements taken every 3 weeks, starting at 6
760 weeks (results presented in Table S3B) (saline n = 14, 4 weeks n = 13, 6 weeks n = 20, 8 weeks n = 20,
761 *Npc1*$^{+/+}$ n = 21). **(C)** Week at which mice reached peak weight (Kruskal-Wallis test with Dunn's multiple

comparisons test). **(D)** Percent weight change between 6 and 9 weeks old (One-way ANOVA with Tukey's multiple comparisons test). For C, D (saline n = 15, 4-week n = 24, 6-week n = 20, 8-week n = 20) for D (*Npc1*$^{+/+}$ n = 21). For all: * $p < 0.05$, ** $p < 0.01$, *** $p < 0.001$, **** $p < 0.0001$. Data presented as mean ± SD for B, C, D.

Figure 6: Age of treatment affects AAV9 transduction in cerebellum and treatment at 4 weeks reduces cerebellar pathology.
(A) ddPCR was used to measure h*NPC1* copy number in the cerebellum of mice at 9 weeks old (Kruskal-Wallis test with Dunn's multiple comparisons test) (saline n = 6, 4 weeks n = 6, 6 weeks n = 4, 8 weeks n = 4, *Npc1*$^{+/+}$ n = 4). (**B**) NPC1 protein levels were assessed via western blot in 9-week-old mice to confirm amount of NPC1 protein in the cerebellum (Kruskal-Wallis test with Dunn's multiple comparisons test) (saline n = 3, 4-week n = 6, 6-week n = 4, 8-week n = 4, *Npc1*$^{+/+}$ n = 4). (**C**) Representative immunofluorescence staining in free floating section for Purkinje neurons, insets are of anterior lobules (IV/V). (**D**) Representative immunofluorescence staining in formalin-fixed, paraffin embedded sections for microgliosis. Insets are of posterior lobules (lobule IX). For C,D: scale bar = 1000 microns for panels, 250 microns for insets. **(E, F, G)** Protein levels for Calbindin (E), CD68 (F), GFAP (G) were assessed via western blot for each 9-week-old mice cohort (Kruskal-Wallis test with Dunn's multiple comparisons test) (saline n = 3, 4 weeks n = 3, 6 weeks n = 4, 8 weeks n = 4, *Npc1*$^{+/+}$ n = 4). For all: * $p < 0.05$, ** $p < 0.01$, *** $p < 0.001$, **** $p < 0.0001$. Data presented as mean ± SD for A, B, E, F, G.

Figure 7: Age of treatment impacts AAV9 transduction in cerebrum and liver and hepatic pathology.
(A, C) ddPCR was used to measure h*NPC1* copy number in mice at 9-weeks old in cerebrum (**A**) and liver (**C**) (Kruskal-Wallis test with Dunn's multiple comparisons test). For A: (saline n = 6, 4 weeks n = 3, 6 weeks n = 4, 8 weeks n = 4, *Npc1*$^{+/+}$ n = 4), for C: (saline n = 6, 4 weeks n = 4, 6 weeks n = 4, 8 weeks n = 4, *Npc1*$^{+/+}$ n = 4). **(B, D)** Linear regression of h*NPC1* copy number in end stage mice in cerebrum (**B)** and liver **(D)**. For B: (saline n = 14, 4 weeks n = 19, 6 weeks n = 20, 8 weeks n = 20, *Npc1*$^{+/+}$ n = 17), for D: (saline n = 14, 4 weeks n = 18, 6 weeks n = 20, 8 weeks n = 20, *Npc1*$^{+/+}$ n = 17). **(E)** Representative immunohistochemical staining of macrophages in the liver in 9-week-old mice (free-floating sections). Scale bar = 250 microns. **(F)** Quantification of percent area CD68 labelled in 9-week-old mice (Kruskal-Wallis test with Dunn's multiple comparisons test) (saline n = 6, 4 weeks n = 8, 6 weeks n = 4, 8 weeks n = 4, *Npc1*$^{+/+}$ n = 4). For all: * $p < 0.05$, ** $p < 0.01$, *** $p < 0.001$, **** $p < 0.0001$. Data presented as mean ± SD for A, C, F.

Figure 8: *Npc1*^{I1061T} mice treated with AAV9 show increased lifespan and delayed disease progression.
(A) Kaplan Meier curve depicts survival of saline injected *Npc1*^{I1061T} mice and *Npc1*^{I1061T} mice treated with AAV9 at 4 weeks. **(B)** Composite phenotype score for each group was measured from 6 to 21 weeks of age at 3-week intervals. **(C)** Week mice reached peak weight (Mann-Whitney test). **(D)** Percent weight change from 10 to 14 weeks (Kruskal-Wallis with Dunn's multiple comparisons). For A, B, C, D (saline n = 11, treated n = 15) and for B,D (*Npc1*$^{+/+}$ n = 15). For all: * $p < 0.05$, ** $p < 0.01$, *** $p < 0.001$, **** $p < 0.0001$. For B, C, D: data presented as mean ± SD.

Figure 9: AAV9 treatment effectively transduces the cerebellum of *Npc1*^{I1061T} mice, modestly impacts cerebellar pathology.
(A) ddPCR was used to measure h*NPC1* copy number in the cerebellum in mice at 14-weeks old (Kruskal-Wallis test with Dunn's multiple comparisons test) (saline n = 4, AAV9 n = 5, *Npc1*$^{+/+}$ n = 4). (**B**) NPC1 protein levels were assessed via western blot in 14-week-old mice to determine amount of NPC1 protein in the cerebellum (Kruskal-Wallis test with Dunn's multiple comparisons test) (saline n = 4, AAV9 n = 5, *Npc1*$^{+/+}$ n = 5). (**C**) Representative immunofluorescence staining in free floating section for Purkinje neurons, insets are of anterior lobules (IV/V). (**D**) Representative immunofluorescence staining in formalin-fixed, paraffin embedded sections for microgliosis. Insets are of posterior lobules (lobule IX). For C,D:

813 scale bar = 1000 microns for panels, 250 microns for insets. **(E, F, G)** Protein levels for Calbindin (E),
814 CD68 (F), GFAP (G) were assessed via western blot for each 9-week-old mice cohort (Kruskal-Wallis test
815 with Dunn's multiple comparisons test) (saline n = 4, AAV9 n = 5, *Npc1*$^{+/+}$ n = 5). For all: * $p < 0.05$, **
816 $p < 0.01$, *** $p < 0.001$, **** $p < 0.0001$. Data presented as mean ± SD for A, B, E, F, G.
817
818 **Figure 10: Transduction efficacy of AAV9 in *Npc1*^{I1061T} mice cerebrum and liver tissue and hepatic**
819 **pathology.**
820 (**A, C**) ddPCR was used to measure h*NPC1* copy number at 14 weeks in cerebrum (**A**) and liver (**C**). For
821 A,C: (Kruskal-Wallis test with Dunn's multiple comparisons test) (saline n = 4, treated n = 5, *Npc1*$^{+/+}$ n =
822 5). (**B, D**) Linear regression of h*NPC1* copy number and lifespan in cerebrum (**B**) or liver (**D**). For B: (saline
823 n = 11, treated n = 12, *Npc1*$^{+/+}$ n = 14), D: (saline n = 11, treated n = 13, *Npc1*$^{+/+}$ n = 14). **(E)** Representative
824 immunohistochemical staining of macrophages in liver of saline-injected, treated, and *Npc1*$^{+/+}$ mice at 14
825 weeks (free floating sections). Scale bar = 250 microns. (**F**) Quantification of percent area CD68 labelled
826 in 14-week-old mice (Kruskal-Wallis test with Dunn's multiple comparisons test) (saline n = 5, treated n =
827 5, *Npc1*$^{+/+}$ n = 6). For all: * $p < 0.05$, ** $p < 0.01$, *** $p < 0.001$, **** $p < 0.0001$. For A, C, F: data
828 presented as mean ± SD.
829

830

SUPPLEMENTAL

Table S1: Antibodies used for immunohistochemical and immunofluorescence staining along with manufacturer and dilution information.

Table S2: Median survival of *Npc1*^{m1N} mice treated with AAV9. Table of median survival for each dose treatment group **(A,** analysis of Fig 1A**)** and each age of treatment group **(B,** analysis of Fig 5A**).** Level of significance is p = 0.0083 based on Bonferroni's correction with 6 comparisons.

Table S3: *Npc1*^{m1N} mice treated with AAV9 vector and *Npc1*$^{+/+}$ mice phenotype score comparison from 6-12 weeks. Two-way ANOVA with mixed effects analysis and Tukey's multiple comparisons test of various dose treatment groups (**A**) and various age treatment groups (**B**) from 6-9 weeks, and 9-12 weeks. Level of significance is p = 0.0083 based on Bonferroni's correction with 6 comparisons.

Table S4: Total sample size for weight curves of each sub study. (**A**) Sample size for male and female mice per treatment group included in dosing study. (**B**) Sample size for male and female mice per treatment group included in age at injection study. (**C**) Sample size for male and female mice per treatment group included in the hypomorphic I1061T study.

S1: Mouse weights. *Npc1*^{m1N} mice treated with AAV9 vector and *Npc1*$^{+/+}$ mice weights over lifespan. Weights are presented as mean ± SD. For the dose study, **(A)** males, **(B)** females. For age at injection: **(C)** males, **(D)** females. For *Npc1*^{I1061T} mice: **(E)** males, **(F)** females. (n) listed in Table S4.

S2: h*NPC1* copy number in tissues of 10-week-old mice treated with varying doses. Gene copy numbers were measured for various organs at 10-weeks-old for *Npc1*^{m1N} mice treated with saline or AAV9 vector at low, medium, and high doses, and untreated *Npc1*$^{+/+}$ mice. Data presented as mean ± SD.

S3: Representative western blots: quantification of NPC1 in cerebrum and liver of *Npc1*^{m1N} mice in dose study.
Representative western blots for quantification of NPC1 in cerebellum **(A)**, quantification shown in Fig 2Aii. Source images for cerebellum **(B)**, right half of blot enlarged in (A). Representative blots for quantification of NPC1 in cerebrum **(C)**, quantification shown in Fig 2Bii. Source images for cerebrum **(D)**, left half of blot enlarged in (C). Representative western blots for quantification of NPC1 in liver **(E)**, quantification shown in Fig 2Cii. Source image for liver **(F)**, right half of blot enlarged in (E). Red box and triangle denote immunoreactive NPC1 protein (~180kDa), black triangle indicates Beta-actin (42kDa). h*NPC1* copy number provided for each sample below (A, C, E). For (D), molecular weight markers are faint in this representative blot; approximate molecular weights were determined from a parallel blot.

S4. Representative western blots: quantification of GFAP, CD68, and Calbindin D in cerebellum of *Npc1*^{m1N} mice in dose study.
Representative western blot for quantification of GFAP **(A)** and CD68 **(C)**, quantification shown in Fig 3C. Source image for GFAP and CD68 **(B)**, right half of blot enlarged in (A, GFAP and C, CD68). Representative western blot for quantification of Calbindin D **(D)**, quantification shown in Fig 3D. Source image for Calbindin D **(E)**, left half of blot enlarged in (D). Brown box and triangle denote GFAP protein (50kDa), purple box and triangle denote CD68 protein (~100 kDa), yellow triangle denotes Calbindin D (28kDa), and black triangle indicates Beta-actin (42kDa). h*NPC1* copy number provided for each sample below blots.

S5: AAV9 modulates sphingolipid accumulation in the brains of *Npc1*^{m1N} mice.
(A) Mass spectrometry imaging of brain of 10-week-old mice treated with varying doses of AAV9. Lipids displayed include **i)** Ganglioside GM2 (d18:1/18:0), **ii)** Hexosylceramide HexCer 46:4;O3, and **iii)**

882 Dihydroceramide Cer 32:2;O3 (for all groups, n = 3, 4-6 sections assessed). **(B)** Quantification of total ion
883 count (TIC) normalized peak areas for GM2 in cerebellum of 10-week-old mice (Kruskal-Wallis test with
884 Dunn's multiple comparisons test).
885
886 **S6: Representative western blots: quantification of NPC1, Calbindin D, CD68, and GFAP in**
887 **cerebellum in *Npc1^{m1N}* mice in age of treatment study.**
888 Representative western blot for quantification of NPC1 and Calbindin D **(A)**, quantification shown in Fig
889 6B,E respectively. Source image for NPC1, Calbindin D, and Beta-actin **(B)**, left half of blot enlarged in
890 (A). Representative blot for quantification of CD68 and GFAP **(C)**, quantification shown in Fig 6F,G
891 respectively. Source image for CD68 and GFAP **(D)**, left half of blot enlarged in (C). Red box and triangle
892 denote NPC1 protein (~180kDa), yellow triangle denotes Calbindin D (28kDa), purple box and triangle
893 denote CD68 protein (~100kDa), brown box and triangle denote GFAP protein (50kDa), and black triangle
894 indicates Beta-actin (42kDa). h*NPC1* copy number provided for each sample below blots for A, C.
895
896 **S7: Representative western blots: quantification of NPC1, Calbindin D, CD68, and GFAP in**
897 **cerebellum in *Npc1^{I1061T}* mice.**
898 Representative western blot for quantification of NPC1 **(A)** and Calbindin D **(C)**, quantification shown in
899 Fig 9B,E respectively. Source image for NPC1 and Calbindin D **(B)**, left third of blot enlarged in (A, NPC1
900 and C, Calbindin D). Representative blot for quantification of CD68 and GFAP **(D)**, quantification shown
901 in Fig 9F,G respectively. Source image for CD68 and GFAP **(E)**, left third of blot enlarged in (D). Red box
902 and triangle denote NPC1 protein (~180kDa), yellow triangle denotes Calbindin D (28kDa), purple box
903 and triangle denote CD68 protein (~100 kDa), brown box and triangle denote GFAP protein (50kDa), and
904 black triangle indicates Beta-actin (42kDa). h*NPC1* copy number provided for each sample below blots for
905 A, C, D.

906 **REFERENCES**

907 1. Vanier, M.T., *Niemann-Pick diseases.* Handb Clin Neurol, 2013. **113**: p. 1717-21.
908 2. Ory, D.S., *Niemann-Pick type C: a disorder of cellular cholesterol trafficking.* Biochim
909 Biophys Acta, 2000. **1529**(1-3): p. 331-9.
910 3. Sleat, D.E., et al., *Genetic evidence for nonredundant functional cooperativity between*
911 *NPC1 and NPC2 in lipid transport.* Proc Natl Acad Sci U S A, 2004. **101**(16): p. 5886-91.
912 4. Infante, R.E., et al., *Purified NPC1 protein. I. Binding of cholesterol and oxysterols to a*
913 *1278-amino acid membrane protein.* J Biol Chem, 2008. **283**(2): p. 1052-63.
914 5. Vanier, M.T., et al., *Genetic heterogeneity in Niemann-Pick C disease: a study using*
915 *somatic cell hybridization and linkage analysis.* Am J Hum Genet, 1996. **58**(1): p. 118-25.
916 6. Cologna, S.M. and A. Rosenhouse-Dantsker, *Insights into the Molecular Mechanisms of*
917 *Cholesterol Binding to the NPC1 and NPC2 Proteins.* Adv Exp Med Biol, 2019. **1135**: p.
918 139-160.
919 7. Walkley, S.U. and K. Suzuki, *Consequences of NPC1 and NPC2 loss of function in*
920 *mammalian neurons.* Biochim Biophys Acta, 2004. **1685**(1-3): p. 48-62.
921 8. Vanier, M.T., *Niemann-Pick disease type C.* Orphanet J Rare Dis, 2010. **5**: p. 16.
922 9. Patterson, M.C., et al., *Recommendations for the diagnosis and management of*
923 *Niemann-Pick disease type C: an update.* Mol Genet Metab, 2012. **106**(3): p. 330-44.
924 10. Mullard, A., *FDA approves first two drugs for rare Niemann-Pick disease.* Nat Rev Drug
925 Discov, 2024.
926 11. Fields, T., et al., *N-acetyl-L-leucine for Niemann-Pick type C: a multinational double-blind*
927 *randomized placebo-controlled crossover study.* Trials, 2023. **24**(1): p. 361.
928 12. Mengel, E., et al., *Efficacy and safety of arimoclomol in Niemann-Pick disease type C:*
929 *Results from a double-blind, randomised, placebo-controlled, multinational phase 2/3*
930 *trial of a novel treatment.* J Inherit Metab Dis, 2021. **44**(6): p. 1463-1480.
931 13. Patterson, M.C., et al., *Miglustat for treatment of Niemann-Pick C disease: a randomised*
932 *controlled study.* Lancet Neurol, 2007. **6**(9): p. 765-72.
933 14. Ory, D.S., et al., *Intrathecal 2-hydroxypropyl-beta-cyclodextrin decreases neurological*
934 *disease progression in Niemann-Pick disease, type C1: a non-randomised, open-label,*
935 *phase 1-2 trial.* Lancet, 2017. **390**(10104): p. 1758-1768.
936 15. Administration, U.S.F.a.D. *FDA approves first treatment for Niemann-Pick disease type C*.
937 2024 September 25, 2024]; Available from: https://www.fda.gov/news-events/press-
938 announcements/fda-approves-first-treatment-niemann-pick-disease-type-c.
939 16. Patterson, M.C., et al., *Stable or improved neurological manifestations during miglustat*
940 *therapy in patients from the international disease registry for Niemann-Pick disease type*
941 *C: an observational cohort study.* Orphanet J Rare Dis, 2015. **10**: p. 65.
942 17. Solomon, B.I., et al., *Association of Miglustat With Swallowing Outcomes in Niemann-*
943 *Pick Disease, Type C1.* JAMA Neurol, 2020. **77**(12): p. 1564-1568.
944 18. Chandler, R.J., et al., *Systemic AAV9 gene therapy improves the lifespan of mice with*
945 *Niemann-Pick disease, type C1.* Hum Mol Genet, 2017. **26**(1): p. 52-64.
946 19. Cain, J.T., et al., *Gene Therapy Corrects Brain and Behavioral Pathologies in CLN6-Batten*
947 *Disease.* Mol Ther, 2019. **27**(10): p. 1836-1847.

948 20. Bosch, M.E., et al., *Self-Complementary AAV9 Gene Delivery Partially Corrects Pathology*
949 *Associated with Juvenile Neuronal Ceroid Lipofuscinosis (CLN3).* J Neurosci, 2016. **36**(37):
950 p. 9669-82.
951 21. Sondhi, D., et al., *Slowing late infantile Batten disease by direct brain parenchymal*
952 *administration of a rh.10 adeno-associated virus expressing CLN2.* Sci Transl Med, 2020.
953 **12**(572).
954 22. Hudry, E. and L.H. Vandenberghe, *Therapeutic AAV Gene Transfer to the Nervous*
955 *System: A Clinical Reality.* Neuron, 2019. **102**(1): p. 263.
956 23. Bradbury, A.M., et al., *Krabbe disease successfully treated via monotherapy of*
957 *intrathecal gene therapy.* J Clin Invest, 2020. **130**(9): p. 4906-4920.
958 24. Mendell, J.R., et al., *Single-Dose Gene-Replacement Therapy for Spinal Muscular*
959 *Atrophy.* N Engl J Med, 2017. **377**(18): p. 1713-1722.
960 25. Al-Zaidy, S., et al., *Health outcomes in spinal muscular atrophy type 1 following AVXS-*
961 *101 gene replacement therapy.* Pediatr Pulmonol, 2019. **54**(2): p. 179-185.
962 26. Lowes, L.P., et al., *Impact of Age and Motor Function in a Phase 1/2A Study of Infants*
963 *With SMA Type 1 Receiving Single-Dose Gene Replacement Therapy.* Pediatr Neurol,
964 2019. **98**: p. 39-45.
965 27. Gao, J., R.M. Hussain, and C.Y. Weng, *Voretigene Neparvovec in Retinal Diseases: A*
966 *Review of the Current Clinical Evidence.* Clin Ophthalmol, 2020. **14**: p. 3855-3869.
967 28. Russell, S., et al., *Efficacy and safety of voretigene neparvovec (AAV2-hRPE65v2) in*
968 *patients with RPE65-mediated inherited retinal dystrophy: a randomised, controlled,*
969 *open-label, phase 3 trial.* Lancet, 2017. **390**(10097): p. 849-860.
970 29. Tai, C.H., et al., *Long-term efficacy and safety of eladocagene exuparvovec in patients*
971 *with AADC deficiency.* Mol Ther, 2022. **30**(2): p. 509-518.
972 30. Manfredsson, F.P., A.C. Rising, and R.J. Mandel, *AAV9: a potential blood-brain barrier*
973 *buster.* Mol Ther, 2009. **17**(3): p. 403-5.
974 31. Foust, K.D., et al., *Intravascular AAV9 preferentially targets neonatal neurons and adult*
975 *astrocytes.* Nat Biotechnol, 2009. **27**(1): p. 59-65.
976 32. Lykken, E.A., et al., *Recent progress and considerations for AAV gene therapies targeting*
977 *the central nervous system.* J Neurodev Disord, 2018. **10**(1): p. 16.
978 33. Duque, S., et al., *Intravenous administration of self-complementary AAV9 enables*
979 *transgene delivery to adult motor neurons.* Mol Ther, 2009. **17**(7): p. 1187-96.
980 34. Gray, S.J., et al., *Preclinical differences of intravascular AAV9 delivery to neurons and*
981 *glia: a comparative study of adult mice and nonhuman primates.* Mol Ther, 2011. **19**(6):
982 p. 1058-69.
983 35. Bagel, J.H., et al., *Electrodiagnostic testing and histopathologic changes confirm*
984 *peripheral nervous system myelin abnormalities in the feline model of niemann-pick*
985 *disease type C.* J Neuropathol Exp Neurol, 2013. **72**(3): p. 256-62.
986 36. Zincarelli, C., et al., *Analysis of AAV serotypes 1-9 mediated gene expression and tropism*
987 *in mice after systemic injection.* Mol Ther, 2008. **16**(6): p. 1073-80.
988 37. Inagaki, K., et al., *Robust systemic transduction with AAV9 vectors in mice: efficient*
989 *global cardiac gene transfer superior to that of AAV8.* Mol Ther, 2006. **14**(1): p. 45-53.
990 38. Gombash, S.E., et al., *Intravenous AAV9 efficiently transduces myenteric neurons in*
991 *neonate and juvenile mice.* Front Mol Neurosci, 2014. **7**: p. 81.

992 39. Schuster, D.J., et al., *Biodistribution of adeno-associated virus serotype 9 (AAV9) vector*
993 *after intrathecal and intravenous delivery in mouse.* Front Neuroanat, 2014. **8**: p. 42.
994 40. Shen, Z., et al., *Intravenous Administration of an AAV9 Vector Ubiquitously Expressing*
995 *C1orf194 Gene Improved CMT-Like Neuropathy in C1orf194(-/-) Mice.*
996 Neurotherapeutics, 2023. **20**(6): p. 1835-1846.
997 41. Higashi, Y., et al., *Peripheral nerve pathology in Niemann-Pick type C mouse.* Acta
998 Neuropathol, 1995. **90**(2): p. 158-63.
999 42. Xie, C., et al., *AAV9-NPC1 significantly ameliorates Purkinje cell death and behavioral*
1000 *abnormalities in mouse NPC disease.* J Lipid Res, 2017. **58**(3): p. 512-518.
1001 43. Hughes, M.P., et al., *AAV9 intracerebroventricular gene therapy improves lifespan,*
1002 *locomotor function and pathology in a mouse model of Niemann-Pick type C1 disease.*
1003 Hum Mol Genet, 2018. **27**(17): p. 3079-3098.
1004 44. Davidson, C.D., et al., *Improved systemic AAV gene therapy with a neurotrophic capsid in*
1005 *Niemann-Pick disease type C1 mice.* Life Sci Alliance, 2021. **4**(10).
1006 45. Kurokawa, Y., et al., *Gene Therapy in a Mouse Model of Niemann-Pick Disease Type C1.*
1007 Hum Gene Ther, 2021. **32**(11-12): p. 589-598.
1008 46. Hughes, M.P., et al., *A Novel Small NPC1 Promoter Enhances AAV-Mediated Gene*
1009 *Therapy in Mouse Models of Niemann-Pick Type C1 Disease.* Cells, 2023. **12**(12).
1010 47. Pentchev, P.G., et al., *A lysosomal storage disorder in mice characterized by a dual*
1011 *deficiency of sphingomyelinase and glucocerebrosidase.* Biochim Biophys Acta, 1980.
1012 **619**(3): p. 669-79.
1013 48. Morris, M.D., et al., *Lysosome lipid storage disorder in NCTR-BALB/c mice. I. Description*
1014 *of the disease and genetics.* Am J Pathol, 1982. **108**(2): p. 140-9.
1015 49. Shio, H., et al., *Lysosome lipid storage disorder in NCTR-BALB/c mice. II. Morphologic and*
1016 *cytochemical studies.* Am J Pathol, 1982. **108**(2): p. 150-9.
1017 50. Loftus, S.K., et al., *Murine model of Niemann-Pick C disease: mutation in a cholesterol*
1018 *homeostasis gene.* Science, 1997. **277**(5323): p. 232-5.
1019 51. Higashi, Y., et al., *Cerebellar degeneration in the Niemann-Pick type C mouse.* Acta
1020 Neuropathol, 1993. **85**(2): p. 175-84.
1021 52. Wasserstein, M.P., et al., *The future of newborn screening for lysosomal disorders.*
1022 Neurosci Lett, 2021. **760**: p. 136080.
1023 53. Patterson, M.C., et al., *Disease and patient characteristics in NP-C patients: findings from*
1024 *an international disease registry.* Orphanet J Rare Dis, 2013. **8**: p. 12.
1025 54. Gaviglio, A., et al., *Infants with Congenital Diseases Identified through Newborn*
1026 *Screening-United States, 2018-2020.* Int J Neonatal Screen, 2023. **9**(2).
1027 55. Administration, H.R.S. *Niemann-Pick disease*. 2024 September 2024 [cited 2025
1028 January]; Available from: https://newbornscreening.hrsa.gov/conditions/niemann-pick-
1029 disease.
1030 56. Surmeli-Onay, O., et al., *Prenatal-onset Niemann-Pick type C disease with nonimmune*
1031 *hydrops fetalis.* Pediatr Neonatol, 2013. **54**(5): p. 344-7.
1032 57. Kelly, D.A., et al., *Niemann-Pick disease type C: diagnosis and outcome in children, with*
1033 *particular reference to liver disease.* J Pediatr, 1993. **123**(2): p. 242-7.
1034 58. Kumagai, T., et al., *A case of Niemann-Pick disease type C with neonatal liver failure*
1035 *initially diagnosed as neonatal hemochromatosis.* Brain Dev, 2019. **41**(5): p. 460-464.

1036 59. Shammas, H., et al., *Different Niemann-Pick C1 Genotypes Generate Protein Phenotypes*
1037 *that Vary in their Intracellular Processing, Trafficking and Localization.* Sci Rep, 2019.
1038 **9**(1): p. 5292.
1039 60. Landrum, M.J., et al., *ClinVar: public archive of relationships among sequence variation*
1040 *and human phenotype.* Nucleic Acids Res, 2014. **42**(Database issue): p. D980-5.
1041 61. McKay Bounford, K. and P. Gissen, *Genetic and laboratory diagnostic approach in*
1042 *Niemann Pick disease type C.* J Neurol, 2014. **261 Suppl 2**(Suppl 2): p. S569-75.
1043 62. Millat, G., et al., *Niemann-Pick C1 disease: the I1061T substitution is a frequent mutant*
1044 *allele in patients of Western European descent and correlates with a classic juvenile*
1045 *phenotype.* Am J Hum Genet, 1999. **65**(5): p. 1321-9.
1046 63. Guatibonza Moreno, P., et al., *At a glance: the largest Niemann-Pick type C1 cohort with*
1047 *602 patients diagnosed over 15 years.* Eur J Hum Genet, 2023. **31**(10): p. 1108-1116.
1048 64. Gelsthorpe, M.E., et al., *Niemann-Pick type C1 I1061T mutant encodes a functional*
1049 *protein that is selected for endoplasmic reticulum-associated degradation due to protein*
1050 *misfolding.* J Biol Chem, 2008. **283**(13): p. 8229-36.
1051 65. Praggastis, M., et al., *A murine Niemann-Pick C1 I1061T knock-in model recapitulates the*
1052 *pathological features of the most prevalent human disease allele.* J Neurosci, 2015.
1053 **35**(21): p. 8091-106.
1054 66. Yerger, J., et al., *Phenotype assessment for neurodegenerative murine models with*
1055 *ataxia and application to Niemann-Pick disease, type C1.* Biol Open, 2022. **11**(4).
1056 67. Martin, K.B., et al., *Identification of Novel Pathways Associated with Patterned*
1057 *Cerebellar Purkinje Neuron Degeneration in Niemann-Pick Disease, Type C1.* Int J Mol Sci,
1058 2019. **21**(1).
1059 68. Maxfield, F.R. and D. Wustner, *Analysis of cholesterol trafficking with fluorescent probes.*
1060 Methods Cell Biol, 2012. **108**: p. 367-93.
1061 69. Peake, K.B. and J.E. Vance, *Defective cholesterol trafficking in Niemann-Pick C-deficient*
1062 *cells.* FEBS Lett, 2010. **584**(13): p. 2731-9.
1063 70. Baudry, M., et al., *Postnatal development of inflammation in a murine model of*
1064 *Niemann-Pick type C disease: immunohistochemical observations of microglia and*
1065 *astroglia.* Exp Neurol, 2003. **184**(2): p. 887-903.
1066 71. Chiba, Y., et al., *Niemann-Pick disease type C1 predominantly involving the*
1067 *frontotemporal region, with cortical and brainstem Lewy bodies: an autopsy case.*
1068 Neuropathology, 2014. **34**(1): p. 49-57.
1069 72. Cologna, S.M., et al., *Human and mouse neuroinflammation markers in Niemann-Pick*
1070 *disease, type C1.* J Inherit Metab Dis, 2014. **37**(1): p. 83-92.
1071 73. Cougnoux, A., et al., *Microglia activation in Niemann-Pick disease, type C1 is amendable*
1072 *to therapeutic intervention.* Hum Mol Genet, 2018. **27**(12): p. 2076-2089.
1073 74. Walker, D.G. and L.F. Lue, *Immune phenotypes of microglia in human neurodegenerative*
1074 *disease: challenges to detecting microglial polarization in human brains.* Alzheimers Res
1075 Ther, 2015. **7**(1): p. 56.
1076 75. Tomita, M., et al., *Immunohistochemical phenotyping of liver macrophages in normal*
1077 *and diseased human liver.* Hepatology, 1994. **20**(2): p. 317-25.
1078 76. Boenzi, S., et al., *Comprehensive-targeted lipidomic analysis in Niemann-Pick C disease.*
1079 Mol Genet Metab, 2021. **134**(4): p. 337-343.

1080 77. Pergande, M.R., et al., *Lipidomic Analysis Reveals Altered Fatty Acid Metabolism in the*
1081 *Liver of the Symptomatic Niemann-Pick, Type C1 Mouse Model.* Proteomics, 2019.
1082 **19**(18): p. e1800285.
1083 78. Elleder, M., et al., *Niemann-Pick disease type C. Study on the nature of the cerebral*
1084 *storage process.* Acta Neuropathol, 1985. **66**(4): p. 325-36.
1085 79. Zervas, M., K. Dobrenis, and S.U. Walkley, *Neurons in Niemann-Pick disease type C*
1086 *accumulate gangliosides as well as unesterified cholesterol and undergo dendritic and*
1087 *axonal alterations.* J Neuropathol Exp Neurol, 2001. **60**(1): p. 49-64.
1088 80. Tobias, F., K.C. Pathmasiri, and S.M. Cologna, *Mass spectrometry imaging reveals*
1089 *ganglioside and ceramide localization patterns during cerebellar degeneration in the*
1090 *Npc1(-/-) mouse model.* Anal Bioanal Chem, 2019. **411**(22): p. 5659-5668.
1091 81. Maue, R.A., et al., *A novel mouse model of Niemann-Pick type C disease carrying a*
1092 *D1005G-Npc1 mutation comparable to commonly observed human mutations.* Hum Mol
1093 Genet, 2012. **21**(4): p. 730-50.
1094 82. Park, W.D., et al., *Identification of 58 novel mutations in Niemann-Pick disease type C:*
1095 *correlation with biochemical phenotype and importance of PTC1-like domains in NPC1.*
1096 Hum Mutat, 2003. **22**(4): p. 313-25.
1097 83. Davies, J.P. and Y.A. Ioannou, *Topological analysis of Niemann-Pick C1 protein reveals*
1098 *that the membrane orientation of the putative sterol-sensing domain is identical to*
1099 *those of 3-hydroxy-3-methylglutaryl-CoA reductase and sterol regulatory element*
1100 *binding protein cleavage-activating protein.* J Biol Chem, 2000. **275**(32): p. 24367-74.
1101 84. Shieh, P.B., et al., *Safety and efficacy of gene replacement therapy for X-linked*
1102 *myotubular myopathy (ASPIRO): a multinational, open-label, dose-escalation trial.*
1103 Lancet Neurol, 2023. **22**(12): p. 1125-1139.
1104 85. Ong, W.Y., et al., *Neurodegeneration in Niemann-Pick type C disease mice.* Exp Brain Res,
1105 2001. **141**(2): p. 218-31.
1106 86. Vance, J.E. and B. Karten, *Niemann-Pick C disease and mobilization of lysosomal*
1107 *cholesterol by cyclodextrin.* J Lipid Res, 2014. **55**(8): p. 1609-21.
1108 87. Lloyd-Evans, E. and F.M. Platt, *Lipids on trial: the search for the offending metabolite in*
1109 *Niemann-Pick type C disease.* Traffic, 2010. **11**(4): p. 419-28.
1110 88. Pineda, M., M. Walterfang, and M.C. Patterson, *Miglustat in Niemann-Pick disease type*
1111 *C patients: a review.* Orphanet J Rare Dis, 2018. **13**(1): p. 140.
1112 89. Karten, B., et al., *Trafficking of cholesterol from cell bodies to distal axons in Niemann*
1113 *Pick C1-deficient neurons.* J Biol Chem, 2003. **278**(6): p. 4168-75.
1114 90. Carcel-Trullols, J., A.D. Kovacs, and D.A. Pearce, *Cell biology of the NCL proteins: What*
1115 *they do and don't do.* Biochim Biophys Acta, 2015. **1852**(10 Pt B): p. 2242-55.
1116 91. Mukherjee, A.B., et al., *Emerging new roles of the lysosome and neuronal ceroid*
1117 *lipofuscinoses.* Mol Neurodegener, 2019. **14**(1): p. 4.
1118 92. Bach, G., *Mucolipidosis type IV.* Mol Genet Metab, 2001. **73**(3): p. 197-203.
1119 93. Sangster, M.L., et al., *A blood-brain barrier-penetrant AAV gene therapy improves*
1120 *neurological function in symptomatic mucolipidosis IV mice.* Mol Ther Methods Clin Dev,
1121 2024. **32**(2): p. 101269.
1122 94. Rodriguez-Gil, J.L., et al., *Genetic background modifies phenotypic severity and longevity*
1123 *in a mouse model of Niemann-Pick disease type C1.* Dis Model Mech, 2020. **13**(3).

Figure 1

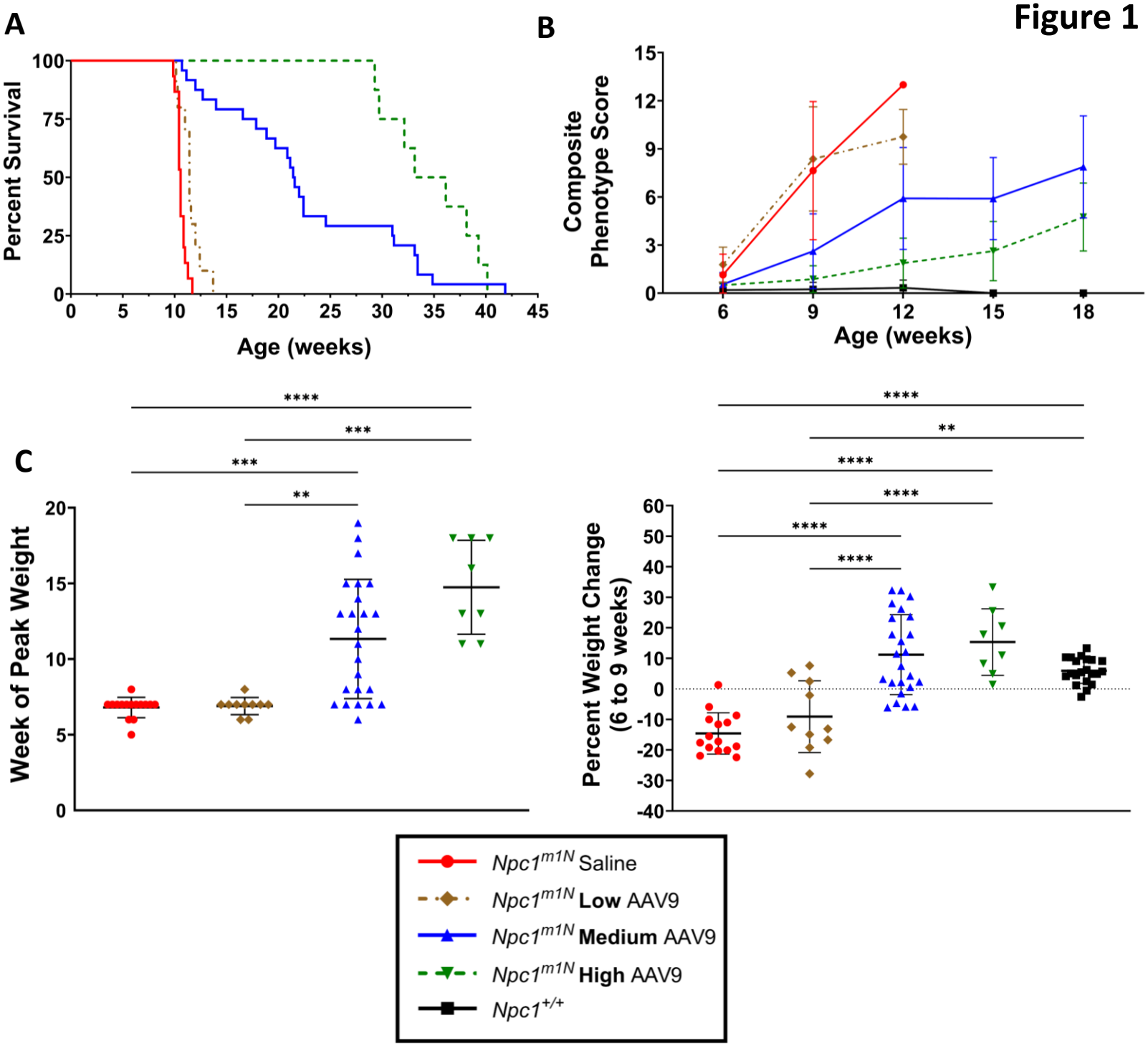
A
Percent Survival
Age (weeks)
B
Composite Phenotype Score
Age (weeks)
C
Week of Peak Weight
Percent Weight Change (6 to 9 weeks)
Npc1m1N Saline
Npc1m1N Low AAV9
Npc1m1N Medium AAV9
Npc1m1N High AAV9
Npc1+/+

Figure 2

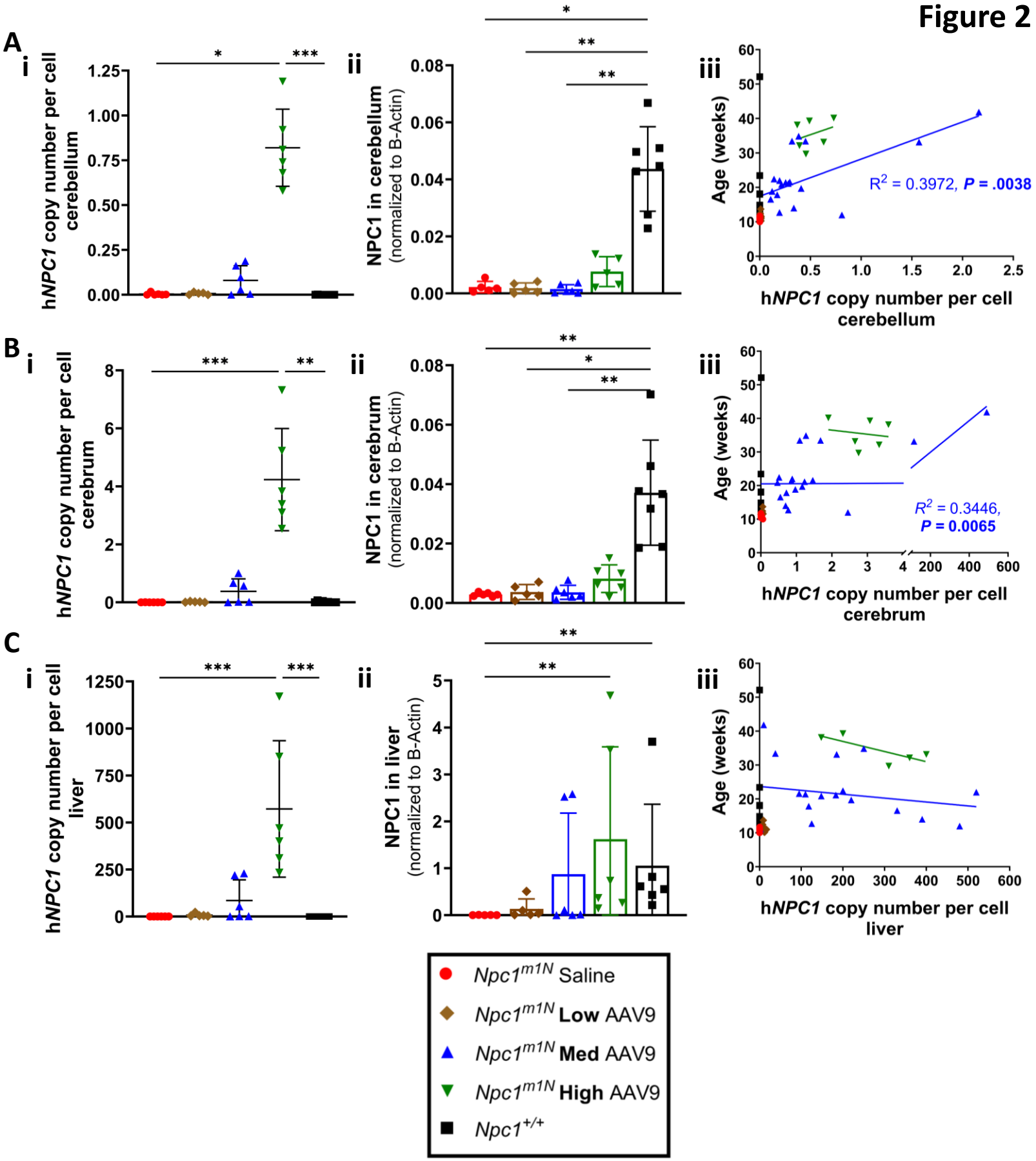
A
i
hNPC1 copy number per cell cerebellum
ii
NPC1 in cerebellum (normalized to B-Actin)
iii
Age (weeks)
R2 = 0.3972, P = .0038
hNPC1 copy number per cell cerebellum
B
i
hNPC1 copy number per cell cerebrum
ii
NPC1 in cerebrum (normalized to B-Actin)
iii
Age (weeks)
R2 = 0.3446, P = 0.0065
hNPC1 copy number per cell cerebrum
C
i
hNPC1 copy number per cell liver
ii
NPC1 in liver (normalized to B-Actin)
iii
Age (weeks)
hNPC1 copy number per cell liver
Npc1m1N Saline
Npc1m1N Low AAV9
Npc1m1N Med AAV9
Npc1m1N High AAV9
Npc1+/+

Figure 3

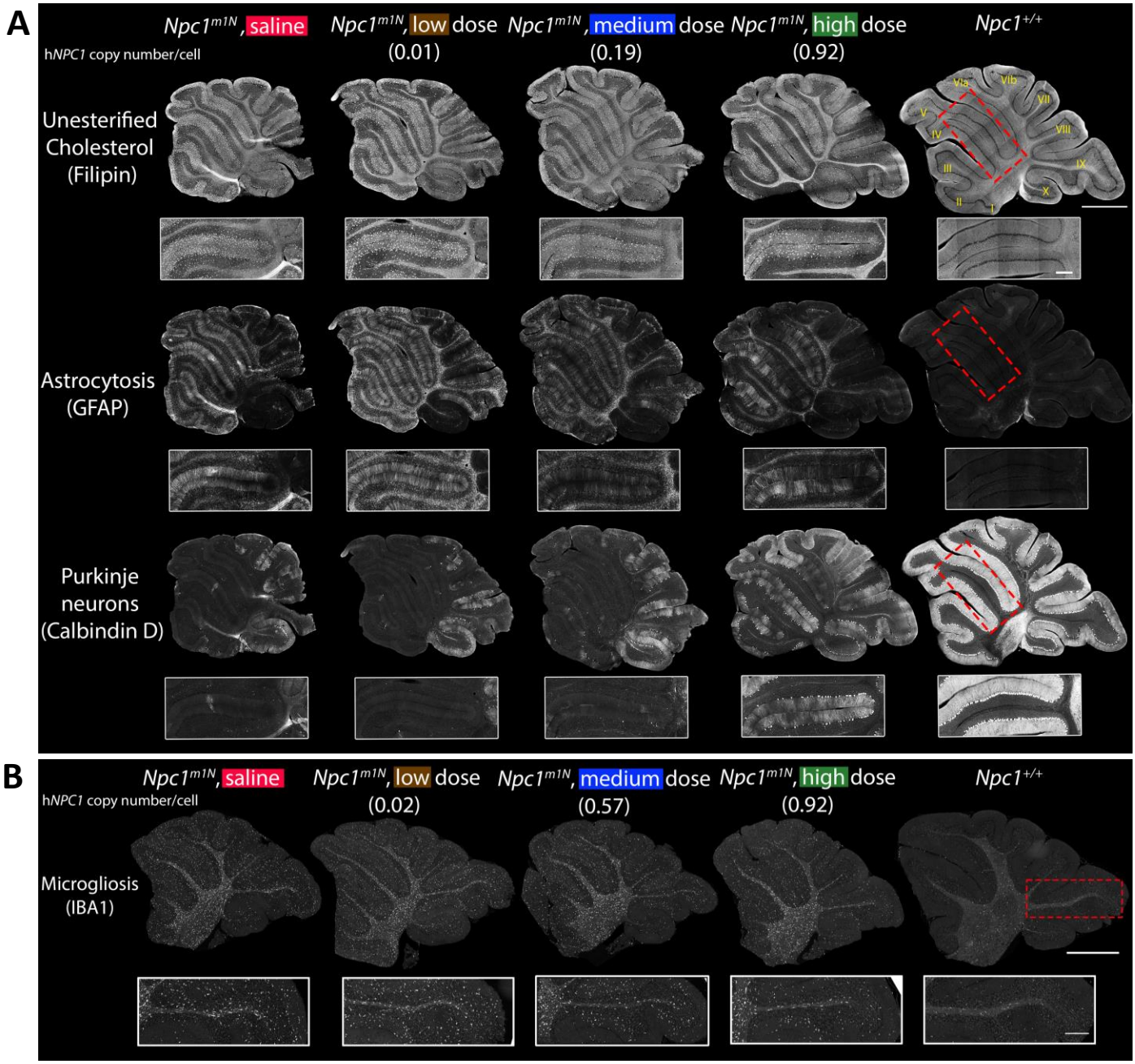
A
Npc1m1N, saline
Npc1m1N, low dose
Npc1m1N, medium dose
Npc1m1N, high dose
Npc1+/+
hNPC1 copy number/cell
(0.01)
(0.19)
(0.92)
Unesterified Cholesterol (Filipin)
Astrocytosis (GFAP)
Purkinje neurons (Calbindin D)
B
Npc1m1N, saline
Npc1m1N, low dose
Npc1m1N, medium dose
Npc1m1N, high dose
Npc1+/+
hNPC1 copy number/cell
(0.02)
(0.57)
(0.92)
Microgliosis (IBA1)

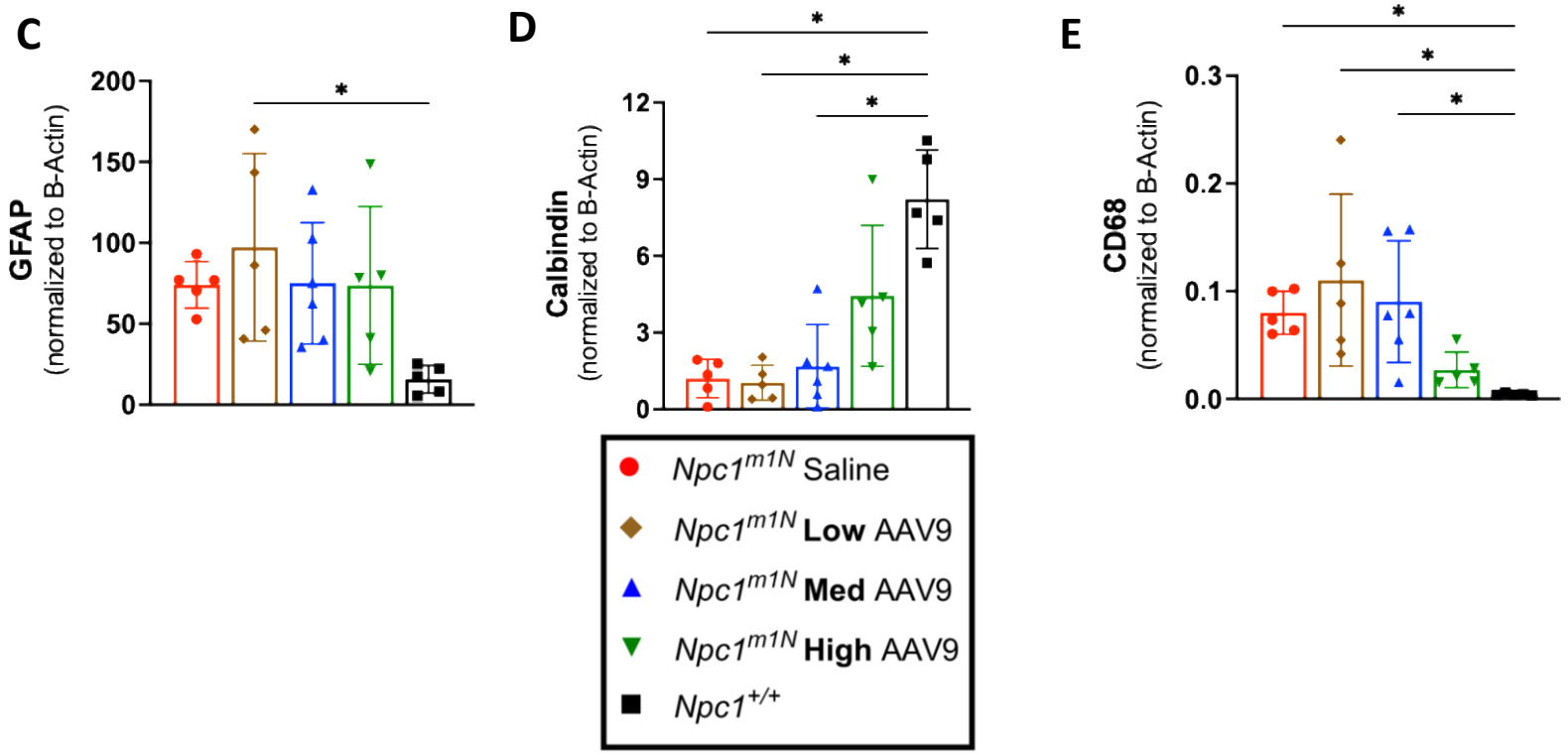
C
GFAP (normalized to B-Actin)
D
Calbindin (normalized to B-Actin)
E
CD68 (normalized to B-Actin)
Npc1m1N Saline
Npc1m1N Low AAV9
Npc1m1N Med AAV9
Npc1m1N High AAV9
Npc1+/+

Figure 4

A

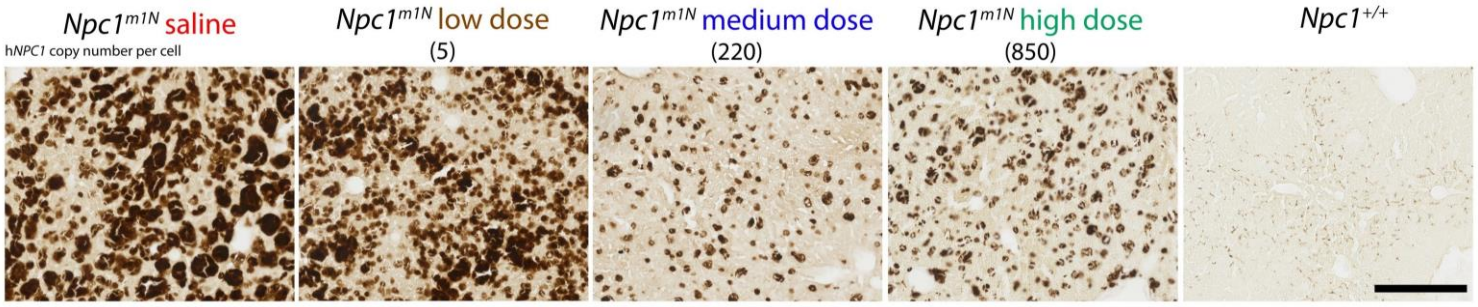
Npc1m1N saline
hNPC1 copy number per cell
Npc1m1N low dose
(5)
Npc1m1N medium dose
(220)
Npc1m1N high dose
(850)
Npc1+/+

B

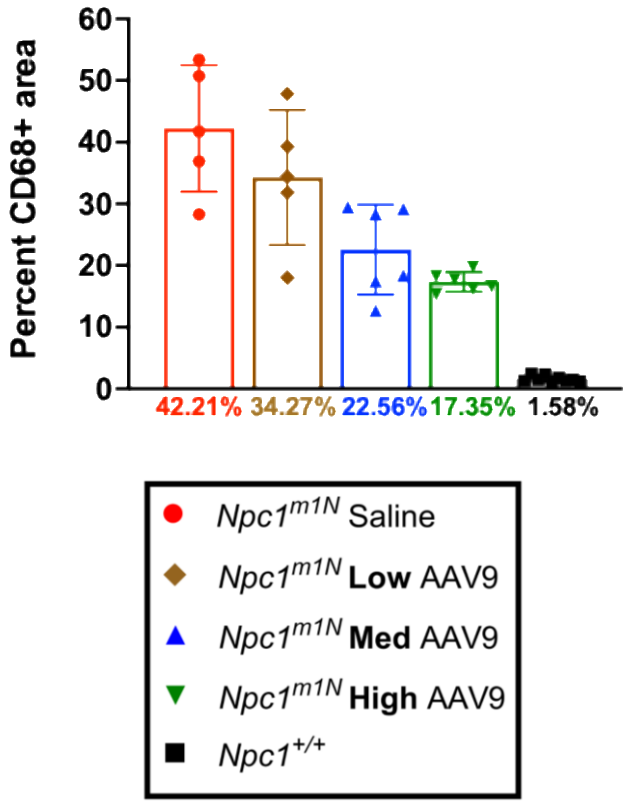
Percent CD68+ area
60
50
40
30
20
10
0
42.21%
34.27%
22.56%
17.35%
1.58%
Npc1m1N Saline
Npc1m1N Low AAV9
Npc1m1N Med AAV9
Npc1m1N High AAV9
Npc1+/+

C

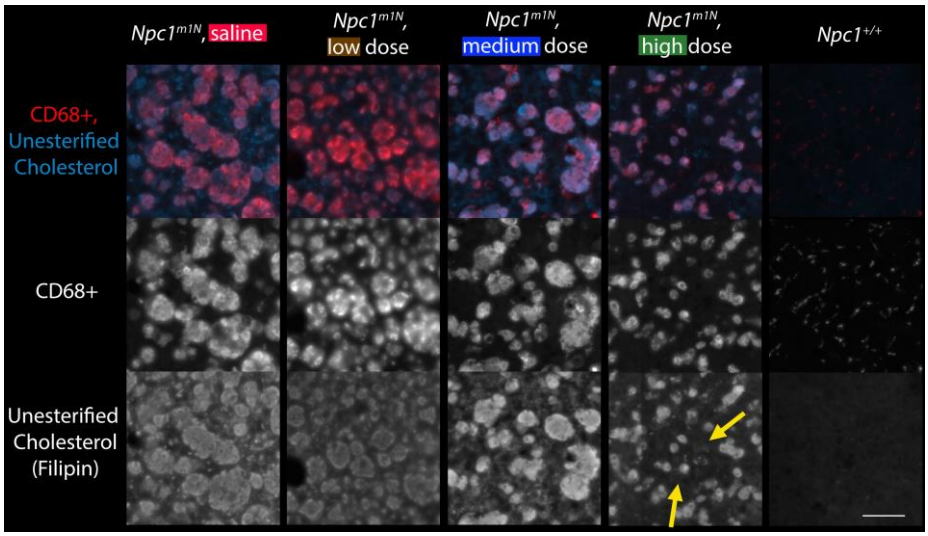
Npc1m1N, saline
Npc1m1N, low dose
Npc1m1N, medium dose
Npc1m1N, high dose
Npc1+/+
CD68+, Unesterified Cholesterol
CD68+
Unesterified Cholesterol (Filipin)

Figure 5

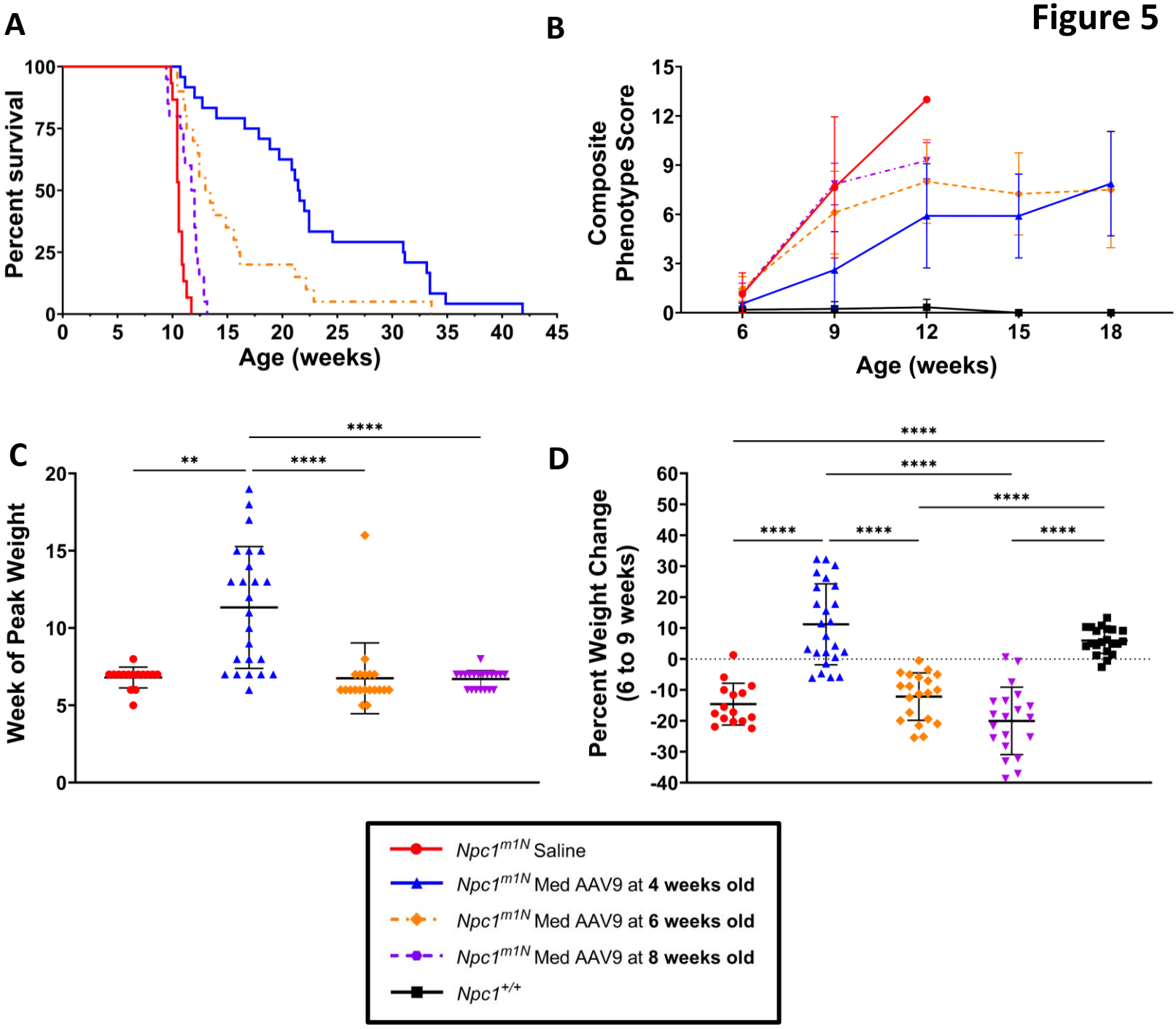
A
Percent survival
Age (weeks)
B
Composite Phenotype Score
Age (weeks)
C
Week of Peak Weight
**
****
****
D
Percent Weight Change (6 to 9 weeks)
****
****
****
****
****
****
Npc1m1N Saline
Npc1m1N Med AAV9 at 4 weeks old
Npc1m1N Med AAV9 at 6 weeks old
Npc1m1N Med AAV9 at 8 weeks old
Npc1+/+

Figure 6

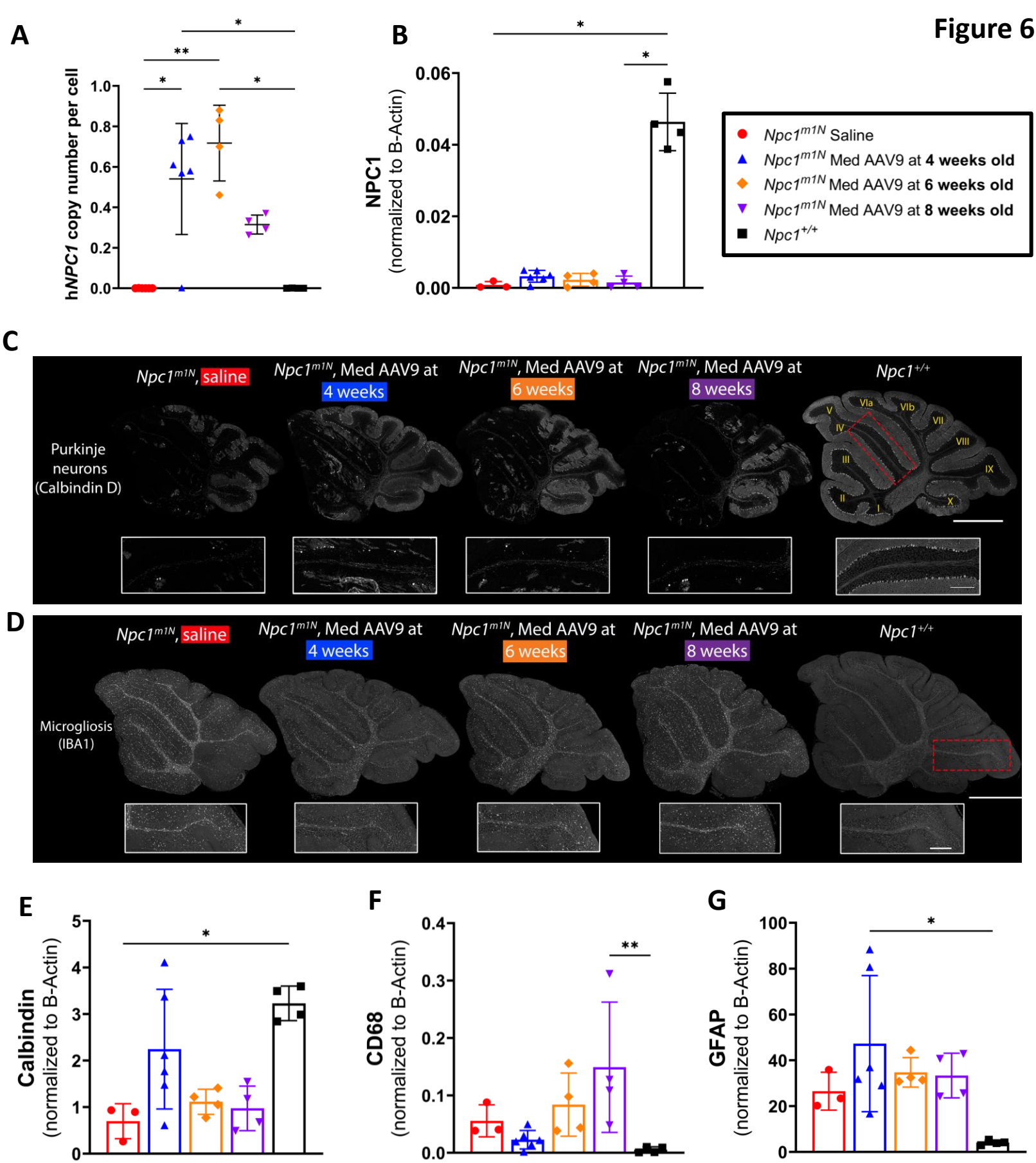
A
hNPC1 copy number per cell
1.0
0.8
0.6
0.4
0.2
0.0
*
**
*
*
B
NPC1
(normalized to B-Actin)
0.06
0.04
0.02
0.00
*
*
Npc1m1N Saline
Npc1m1N Med AAV9 at 4 weeks old
Npc1m1N Med AAV9 at 6 weeks old
Npc1m1N Med AAV9 at 8 weeks old
Npc1+/+
C
Npc1m1N, saline
Npc1m1N, Med AAV9 at 4 weeks
Npc1m1N, Med AAV9 at 6 weeks
Npc1m1N, Med AAV9 at 8 weeks
Npc1+/+
Purkinje neurons (Calbindin D)
V
VIa
VIb
VII
IV
VIII
III
IX
II
I
X
D
Npc1m1N, saline
Npc1m1N, Med AAV9 at 4 weeks
Npc1m1N, Med AAV9 at 6 weeks
Npc1m1N, Med AAV9 at 8 weeks
Npc1+/+
Microgliosis (IBA1)
E
Calbindin
(normalized to B-Actin)
5
4
3
2
1
0
*
F
CD68
(normalized to B-Actin)
0.4
0.3
0.2
0.1
0.0
**
G
GFAP
(normalized to B-Actin)
100
80
60
40
20
0
*

Figure 7

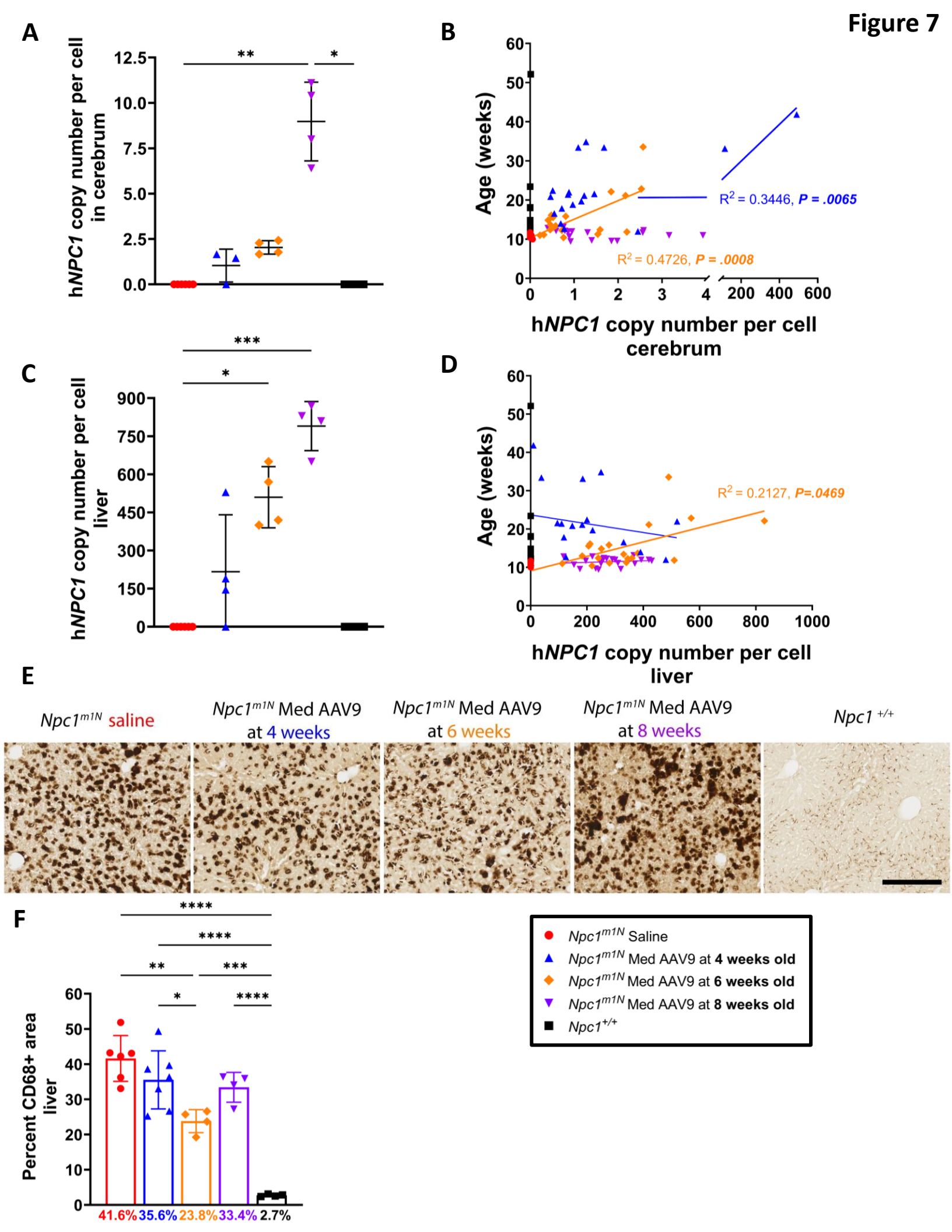
A
hNPC1 copy number per cell in cerebrum
12.5
10.0
7.5
5.0
2.5
0.0
**
*
B
Age (weeks)
60
50
40
30
20
10
0
R2 = 0.3446, P = .0065
R2 = 0.4726, P = .0008
0
1
2
3
4
200
400
600
hNPC1 copy number per cell cerebrum
C
hNPC1 copy number per cell liver
900
750
600
450
300
150
0
***
*
D
Age (weeks)
R2 = 0.2127, P=.0469
0
200
400
600
800
1000
hNPC1 copy number per cell liver
E
Npc1m1N saline
Npc1m1N Med AAV9 at 4 weeks
Npc1m1N Med AAV9 at 6 weeks
Npc1m1N Med AAV9 at 8 weeks
Npc1 +/+
F
Percent CD68+ area liver
60
50
40
30
20
10
0
****
****
**
***
*
****
41.6%
35.6%
23.8%
33.4%
2.7%
Npc1m1N Saline
Npc1m1N Med AAV9 at 4 weeks old
Npc1m1N Med AAV9 at 6 weeks old
Npc1m1N Med AAV9 at 8 weeks old
Npc1+/+

Figure 8

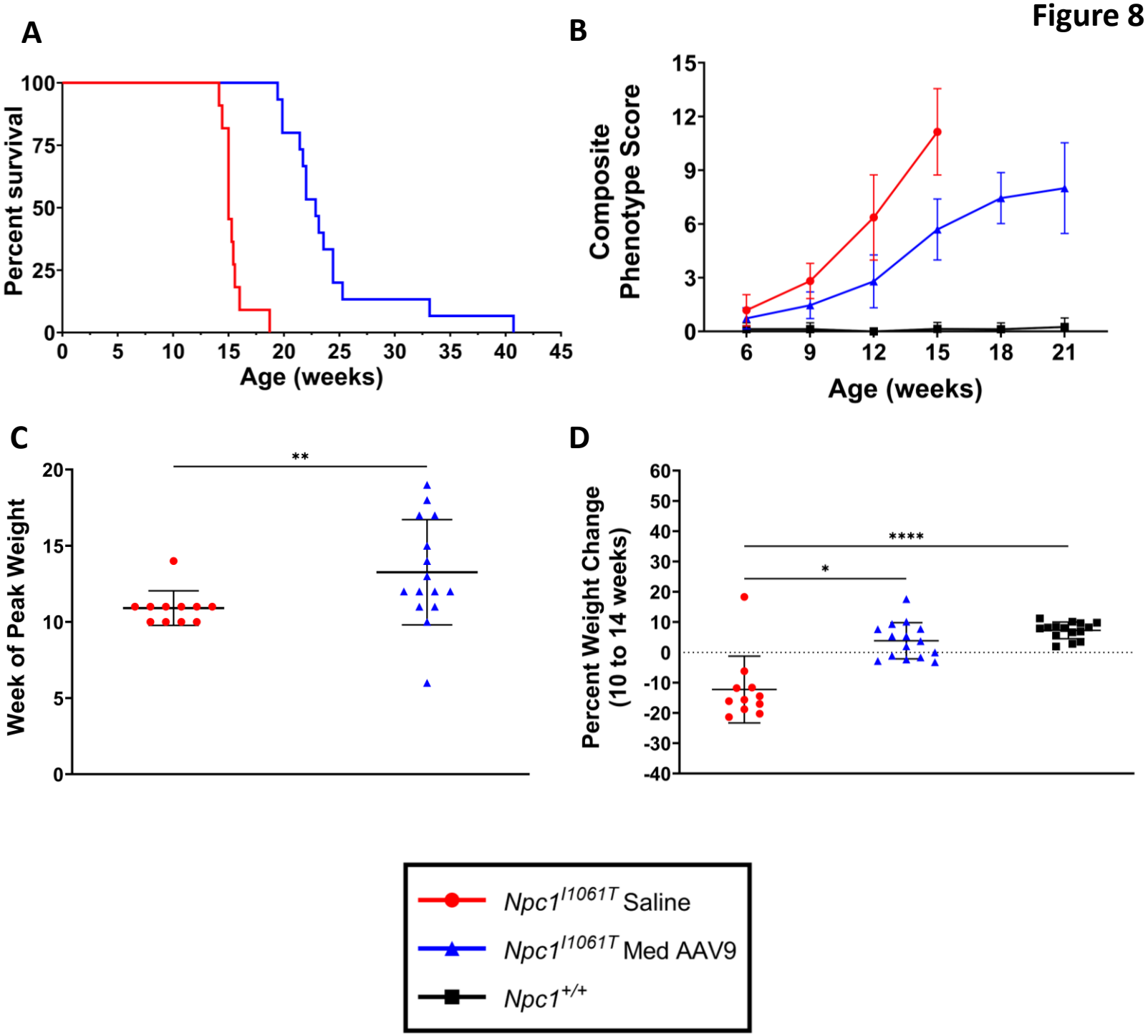
A
Percent survival
100
75
50
25
0
0
5
10
15
20
25
30
35
40
45
Age (weeks)
B
Composite Phenotype Score
15
12
9
6
3
0
6
9
12
15
18
21
Age (weeks)
C
Week of Peak Weight
20
15
10
5
0
**
D
Percent Weight Change (10 to 14 weeks)
60
50
40
30
20
10
0
-10
-20
-30
-40
****
*
Npc1I1061T Saline
Npc1I1061T Med AAV9
Npc1+/+

Figure 9

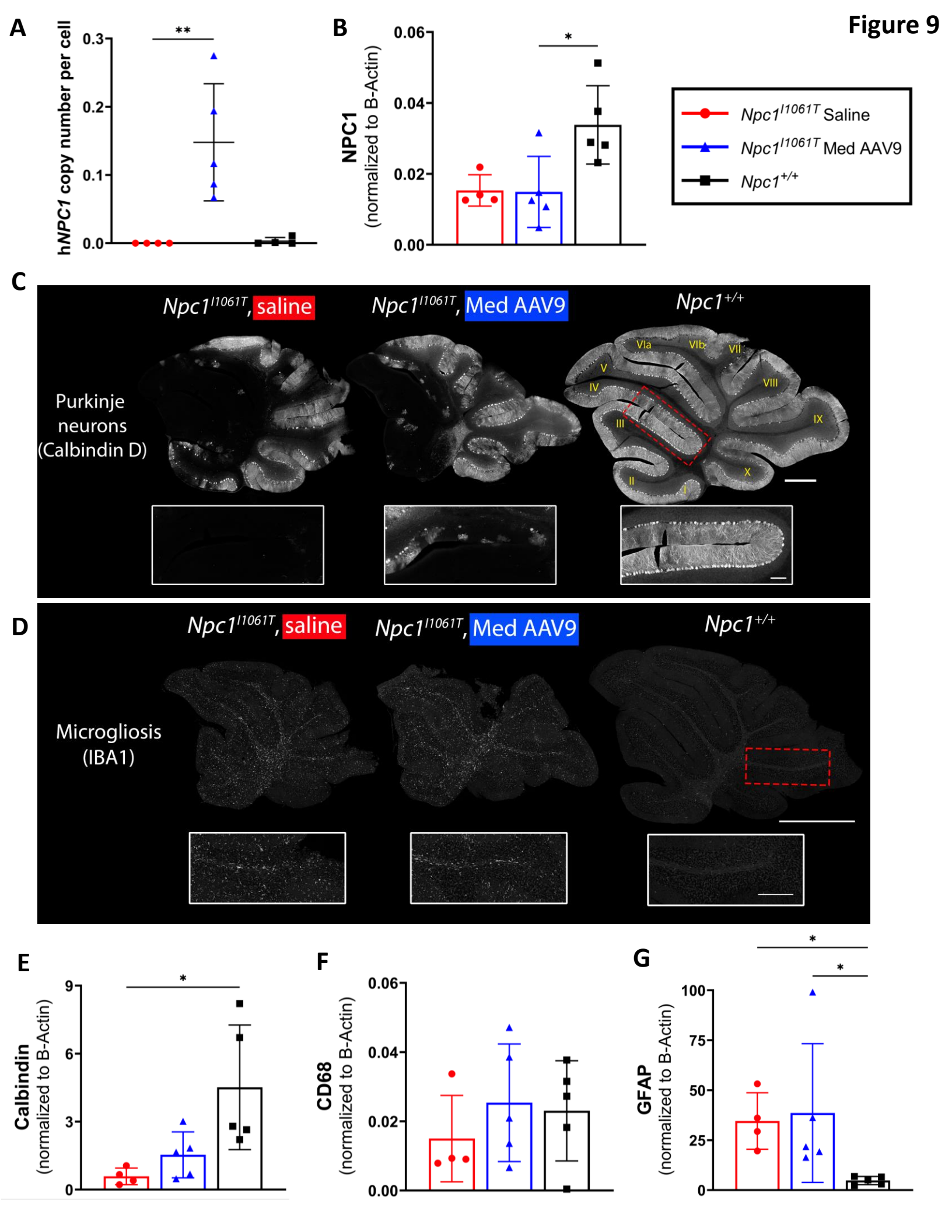
A
hNPC1 copy number per cell
0.3
0.2
0.1
0.0
**
B
NPC1
(normalized to B-Actin)
0.06
0.04
0.02
0.00
*
Npc1I1061T Saline
Npc1I1061T Med AAV9
Npc1+/+
C
Npc1I1061T, saline
Npc1I1061T, Med AAV9
Npc1+/+
Purkinje neurons (Calbindin D)
VIa
VIb
VII
V
IV
VIII
III
IX
II
I
X
D
Npc1I1061T, saline
Npc1I1061T, Med AAV9
Npc1+/+
Microgliosis (IBA1)
E
Calbindin
(normalized to B-Actin)
9
6
3
0
*
F
CD68
(normalized to B-Actin)
0.06
0.04
0.02
0.00
G
GFAP
(normalized to B-Actin)
100
75
50
25
0
*
*

Figure 10

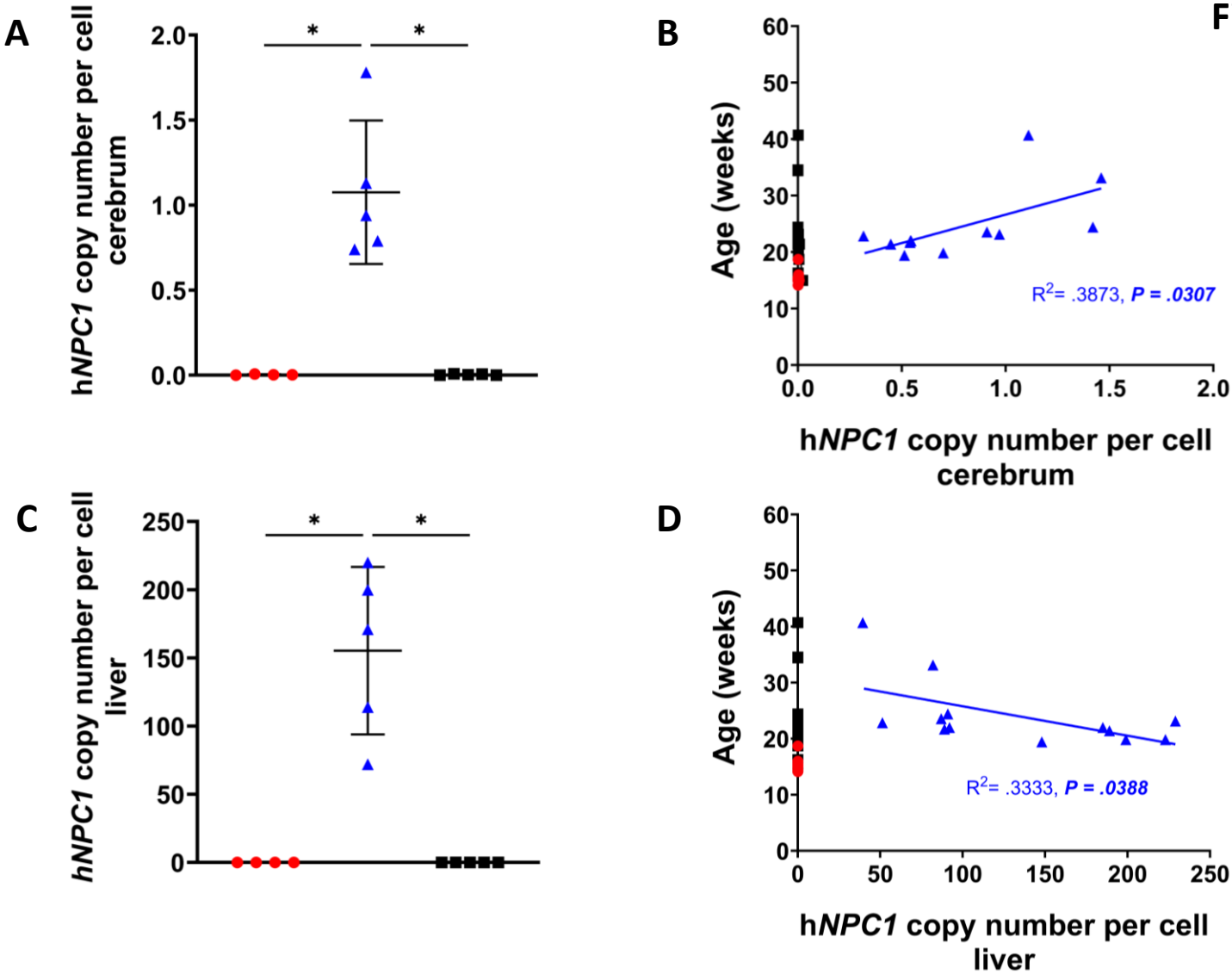
A
hNPC1 copy number per cell cerebrum
2.0
1.5
1.0
0.5
0.0
*
*
B
Age (weeks)
60
50
40
30
20
10
0
0.0
0.5
1.0
1.5
2.0
R2= .3873, P = .0307
hNPC1 copy number per cell cerebrum
C
hNPC1 copy number per cell liver
250
200
150
100
50
0
*
*
D
Age (weeks)
60
50
40
30
20
10
0
0
50
100
150
200
250
R2= .3333, P = .0388
hNPC1 copy number per cell liver

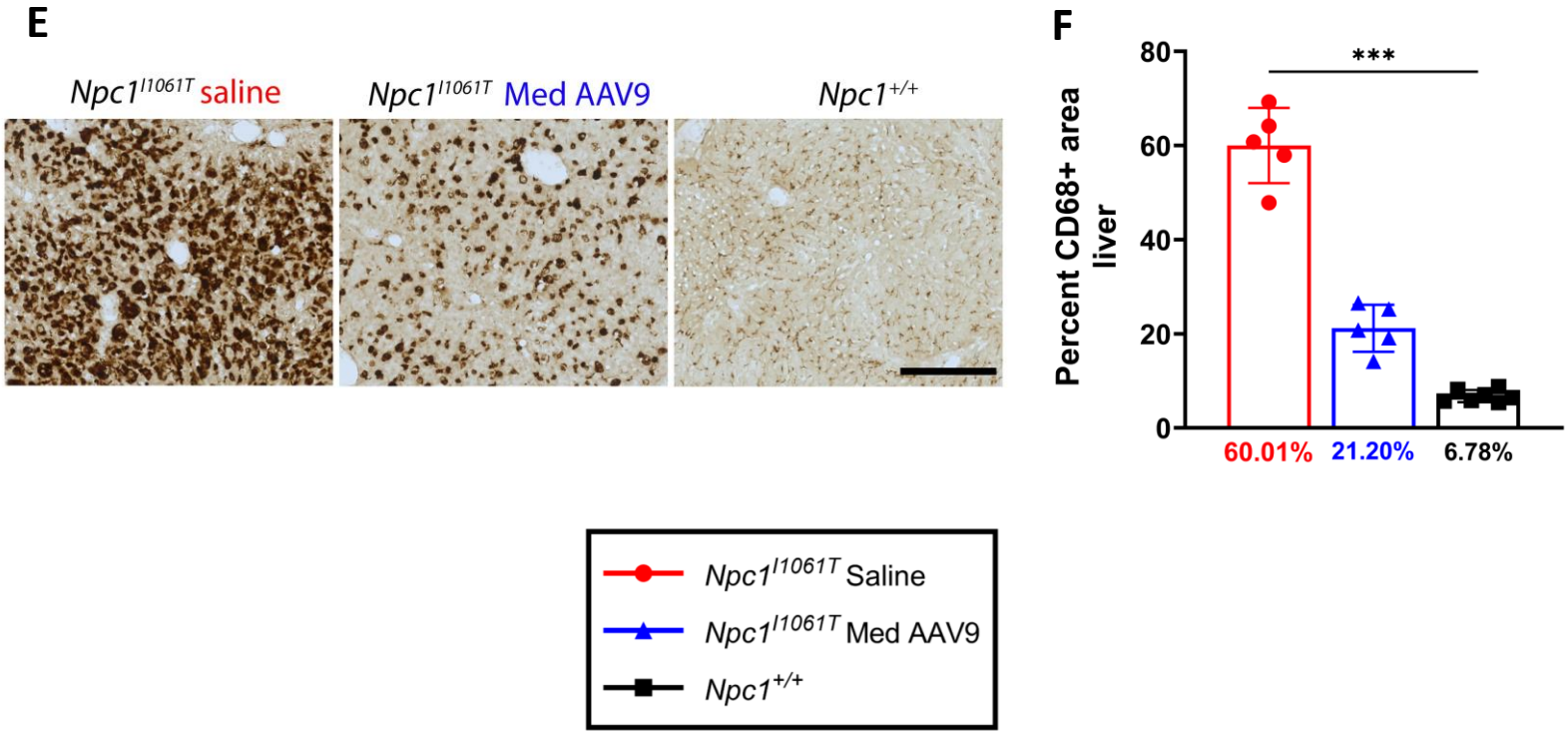
E
Npc1I1061T saline
Npc1I1061T Med AAV9
Npc1+/+
F
Percent CD68+ area liver
80
60
40
20
0
***
60.01%
21.20%
6.78%
Npc1I1061T Saline
Npc1I1061T Med AAV9
Npc1+/+